The Astrophysical Journal, 889:34 (25pp), 2020 January 20 https://doi.org/10.3847/1538-4357/ab5d2f

Electron-capture Supernovae of Super-AGB Stars: Sensitivity on Input Physics

Shing-Chi Leung[1,2], Ken'ichi Nomoto[1], and Tomoharu Suzuki[3]
[1] Kavli Institute for the Physics and Mathematics of the Universe (WPI), UTIAS, The University of Tokyo, Kashiwa, Chiba 277-8583, Japan
shingchi.leung@ipmu.jp, nomoto@astron.s.u-tokyo.ac.jp
[2] TAPIR, Walter Burke Institute for Theoretical Physics, Mailcode 350-17, Caltech, Pasadena, CA 91125, USA
[3] College of Engineering, Chubu University, 1200 Matsumoto-cho, Kasugai, Aichi 487-8501, Japan; tsuzuki@isc.chubu.ac.jp
Received 2019 January 30; revised 2019 November 26; accepted 2019 November 26; published 2020 January 22

Abstract

Stars of $M \sim 8$–$10\,M_\odot$ on their main sequence form strongly electron-degenerate oxygen–neon–magnesium (ONeMg) cores and become super–asymptotic giant branch stars. If such an ONeMg core grows to $1.38\,M_\odot$, electron captures on ^{20}Ne$(e, \nu_e)^{20}$F$(e, \nu_e)^{20}$O take place and ignite O–Ne deflagration around the center. In this work, we perform two-dimensional hydrodynamical simulations of the propagation of the O–Ne flame to see whether such a flame triggers a thermonuclear explosion or induces a collapse of the ONeMg core due to subsequent electron capture behind the flame. We present a series of models to explore how the outcome depends on model parameters for a central density ranging between $10^{9.80}$ and $10^{10.20}$ g cm^{-3}, flame structures of both centered and off-centered ignition kernels, special and general relativistic effects, turbulent flame speed formulae, and the treatments of laminar burning phase. We obtain bifurcation between the electron-capture induced collapse and thermonuclear explosion depending mainly on the central density. We find that the ONeMg core obtained from stellar evolutionary models has a high tendency to collapse into a neutron star. We discuss the implications of the electron-capture supernovae in chemical evolution and the possible observational signals of this class of supernovae.

Unified Astronomy Thesaurus concepts: Supernovae (1668); Asymptotic giant branch stars (2100); Hydrodynamical simulations (767); Neutron stars (1108)

1. Introduction

1.1. Formation and Evolution of Degenerate ONeMg Cores

Stars with initial masses $M = 8$–$10\,M_\odot$ have an interesting transition from massive white dwarf (WD) formation (e.g., Sugimoto & Nomoto 1980; Nomoto & Hashimoto 1988; Arnett 1996; Nomoto et al. 2013) to core collapse supernova (CCSN; Sugimoto & Nomoto 1980; Nomoto & Hashimoto 1988; Arnett 1996; Nomoto et al. 2013). Stars with $M < M_{\rm up,C} = 7 \pm 2\,M_\odot$ form a carbon–oxygen (CO) WD (e.g., Nomoto 1982; Umeda & Nomoto 1999; Karakas 2017). Stars with $M > M_{\rm up,C}$, C-burning produces an oxygen–neon–magnesium (ONeMg) core. The helium shell expands and is dredged up by surface convection, which leads to the formation of a sub-Chandrasekhar mass degenerate ONeMg core (Nomoto 1987). The final ONeMg core mass depends on the competition between the core mass growth due to H- and He-shell burning and the loss of the envelope mass (e.g., Siess 2007; Pumo et al. 2009; Langer 2012). For $10\,M_\odot > M > M_{\rm up,Ne} = 9 \pm 1\,M_\odot$, the ONeMg core reaches $\sim 1.4\,M_\odot$ to collapse. For $M_{\rm up,Ne} > M > M_{\rm up,C}$, the ONeMg core becomes a massive ONeMg WD by losing the envelope. For $M > 10\,M_\odot$, off-center Ne burning is ignited in the ONeMg core when the core mass reaches $1.37\,M_\odot$ (Nomoto 1984), which leads to the formation of an Fe core.

For $10\,M_\odot > M > M_{\rm up,Ne}$, once the ONeMg core reaches a central density of 10^9 g cm^{-3}, the odd number isotope pairs (^{25}Mg, ^{25}Na), (^{23}Na, ^{23}Ne), and (^{25}Na, ^{25}Ne) undergo Urca processes (electron captures and β decays, see, e.g., Schwab et al. 2017 for the CO WD case) with their recent rates computed by Toki et al. (2013) and Suzuki et al. (2016). At $10^{9.6}$ g cm^{-3}, electron capture on ^{24}Mg may further create a steep electron fraction Y_e gradient, which may trigger semi-convection. The lowered Y_e makes the core further contract (Miyaji et al. 1980; Nomoto et al. 1982; Nomoto 1987). Meanwhile, electron captures heat the core by its gamma-ray deposition. For the treatment of convection, we can apply both the Schwarzschild criterion (Miyaji et al. 1980; Nomoto 1987; Takahashi et al. 2013; Jones et al. 2014) and the Ledoux criterion (Miyaji & Nomoto 1987; Hashimoto et al. 1993; Jones et al. 2013; Schwab et al. 2015). They give a range of O/Ne ignition densities from $10^{9.95}$ g cm^{-3} (Ledoux criterion) to $10^{10.2}$ g cm^{-3} (Schwarzschild criterion). Note that the density where thermonuclear runaway occurs (runaway density) is higher than the ignition density, because even with the Ledoux criterion, O/Ne burning produces a convectively unstable region, which may delay the nuclear runaway by transporting the nuclear energy from O- and Ne-burning away by convection. In this sense, $10^{9.95}$ g cm^{-3} is the lower limit of the runaway density.

Electron-capture supernovae (ECSNe) are one of the channels for low-mass neutron star (NS) formation, similar to the accretion-induced collapse (Canal & Schatzman 1976). However, the full picture of how such low-mass NSs form remains a matter of debate due to the limited observational constraints (see, e.g., Mochkovitch & Livio 1989; Dessart et al. 2006; Yoon et al. 2007).

1.2. Physics of O–Ne Deflagration

Near the end of the super–asymptotic giant branch (AGB) star evolution, the ONeMg core of can attain a central density $\sim 2 \times 10^9$ K where weak interactions are important (Nomoto 1984). Above $\sim 2 \times 10^9$ K, the burning timescale of O in the core becomes shorter than the hydrodynamical timescale $t_{\rm hyd}$. Then the thermonuclear runaway takes place near the center to form a nuclear deflagration wave (Nomoto et al. 1976; Nomoto 1984; Timmes & Woosley 1992). The rapid electron captures in the burnt ash lower the electron fraction Y_e. The detailed evolution is dependent upon the initial model and related input physics, including the runaway density, position, and geometry of the O–Ne deflagration, the turbulent flame physics and the transition

from laminar flame to turbulent flame regime. Therefore, the final fate of the ECSN is less obvious because electron captures can slow down the propagation of the nuclear flame or can even trigger the collapse. To model the turbulent flame properly, multidimensional simulations are necessary.

Nuclear deflagration has been extensively studied and modeled in the SN Ia literature (Reinecke et al. 1999, 2002a, 2002b; Röpke 2005; Röpke & Hillebrandt 2005; Röpke et al. 2007; Ma et al. 2013; Fink et al. 2014; Long et al. 2014). By electron conduction, the deflagration wave propagates with a sub-sonic velocity and the speed increases with density (Timmes & Woosley 1992). Deflagration is susceptible to fluid advection and hydrodynamical instabilities including Rayleigh–Taylor instabilities, Kelvin–Helmholtz instabilities, and Landau–Derrieius instabilities (Timmes & Woosley 1992; Livne & Arnett 1993; Bell et al. 2004a, 2004b; Röpke et al. 2004a, 2004b). In general, the flame has a complex geometry, and an explicit front-capturing scheme is often essential to accurately describe the evolution of the deflagration wave (Osher & Sethian 1988). Due to the sub-sonic nature of the flame, the burnt matter may have sufficient time to expand and relax isobarically (Khokhlov et al. 1997), which creates a density contrast in the fuel. Matter with a high temperature ($>5 \times 10^9$ K) may release sufficient energy to make the matter enter the nuclear statistical equilibrium (NSE). The photo-disintegration of iron-peak elements in the ash and its further electron capture may also alter the structure of the laminar deflagration wave.

1.3. Motivation

The uncertainties of the input physics in stellar evolution near the ignition of the ONeMg core result in uncertainties of the initial models of ECSN. The uncertainties originate from the needs of an extensive nuclear network for the weak interaction process, the treatment of the Urca process and its associated convection, and the possibility of (semi-)convection near the core before the onset of nuclear runaway. As a result, the ignition density of ECSN, the position, and size of the nuclear runaway are not yet well constrained. Early work shows that the results are sensitive to the ignition density (Gershteĭn et al. 1977; Chechetkin et al. 1980). Furthermore, the results depend on the nature of the turbulent flame (Nomoto & Kondo 1991), where multidimensional simulations are naturally required. The first three-dimensional model of the deflagration phase (Jones et al. 2016) demonstrates the importance of the input physics. Their models show that the Coulomb corrections in the equation of state can result in different explosion strengths. The choices of the convection criteria, which affect the ignition density, can also alter the final explosion strength. In Jones et al. (2019), the nucleosynthesis based on their previous work is computed with a large nuclear network including 5234 isotopes. Their models can reproduce features of a recently observed Mn-enhanced low-mass WD LP 40-365 (Raddi et al. 2018). These results inspire us to examine carefully the role of the initial model and various input physics of the ECSN to determine the final fate of the ECSN. We use the two-dimensional hydrodynamical code for the computation. Two-dimensional models allow us to explore the parameter space systematically in reasonable computational time.

In Section 2, we briefly outline our hydrodynamical code and the updates employed to model the pre-collapse phase. In Section 3, we present our parameter study, which includes an array of models that follow the evolution of ONeMg cores with different configurations. This aims at studying the post-runaway evolution of the ONeMg core at different (1) central densities, (2) initial flame structures, (3) initial flame positions, (4) gravity models, (5) flame physics, (6) pre-runaway configurations, and (7) initial composition. In Section 4, we discuss how our results can be understood collectively for future models given by stellar evolution. We also compare our results with the representative models in the literature. Then, we discuss the possible observational constraints on ECSN. At last, we present our conclusions. In the Appendix, we provide the resolution study of our ECSN models. We also present briefly the possible observational consequences when the ECSN collapses to form an NS by carrying out one-dimensional simulations with neutrino transport (the advanced leakage scheme).

Table 1
Comparison between the Input Physics of ECSN and Type Ia Supernova

Input physics	ECSN	Type Ia supernova
Central density	$\sim 10^{10}$ g cm^{-3}	10^7–10^{10} g cm^{-3}
Mass	1.38	0.9–1.38
Y_e range	0.37–0.50	0.44–0.50
Composition	ONe-rich matter	CO-rich matter
Peak temperature	$\sim 10^{10}$ K	$\sim 10^{10}$ K
Energy production	ONe- and Si-burning and NSE	CO-burning, Si-burning and NSE
Electron capture	NSE matter	NSE matter

2. Methods

We use the two-dimensional hydrodynamics code developed for supernovae and nucleosynthesis. We refer readers to Leung et al. (2015a, 2015b), Leung & Nomoto (2017, 2018), and Nomoto & Leung (2017b) for a detailed description of the code and its previous applications. We also refer the readers to Nomoto & Leung (2017a) for the evolutionary path of an ECSN before the onset of nuclear runaway. In general, the input physics of an ECSN is similar to an SN Ia, since nuclear reactions and electron captures are the principle input physics. In Table 1, we tabulate the governing physics and their typical values for these two types of simulations to characterize the principle similarities and differences.

2.1. Hydrodynamics

The code solves the Euler equations in the cylindrical coordinates. The simulation box uses a uniform 400×400 grid mesh with a size $\sim$4 km in both the r- and z-directions. The Courant factor is chosen to be 0.25. Only a quadrant of the sphere is modeled where the inner (outer) boundaries are chosen to be reflective (outgoing). We use the fifth-order weighted-essentially non-oscillatory (WENO) scheme for the spatial discretization (Barth & Deconinck 1999) and the five-step third-order non-strong stability-preserving Runge–Kutta (NSSP-RK) scheme (Wang & Spiteri 2007) for the time discretization. We use the Helmholtz equation of state (Timmes & Arnett 1999). This equation of state includes the contributions of an ideal electron gas at arbitrarily degenerate and relativistic levels, ions in the form of a classical ideal gas, photons with the Planck distribution and the electron-positron pairs. The level-set method is used for tracking the flame geometry inside the ECSN.

We use the same turbulent flame prescription used in our SN Ia work. The effective flame propagation speed is a function of

the laminar flame speed $v_{\rm lam}$ and the local velocity fluctuations due to turbulence v' (see also Pocheau 1994; Niemeyer et al. 1995; Schmidt et al. 2006; Leung et al. 2015a for the general formulation of a turbulent nuclear flame). In this work, we choose the flame models proposed in Schmidt et al. (2006). The laminar speed is a function of density and ^{16}O mass fraction given in Timmes & Woosley (1992). The one-equation model (Niemeyer et al. 1995) is used for modeling the growth and the decay of sub-grid scale turbulence. We define the specific kinetic energy density in the sub-grid scale $q_{\rm turb} = |\boldsymbol{v}'|^2/2$. This energy density is a scalar that follows fluid advection and exchanges energy with the internal energy of the fluid. Depending on the context, the source terms of sub-grid turbulence $\dot{q}_{\rm turb}$ can contain different terms. In a star, $\dot{q}_{\rm turb} = \dot{q}_{\rm prod} + \dot{q}_{\rm diss} + \dot{q}_{\rm comp} + \dot{q}_{\rm RT} + \dot{q}_{\rm diff}$. The terms on the right-hand side stand for the source terms by shear stress, turbulence dissipation, turbulence production by compression, Rayleigh–Taylor instabilities, and turbulent diffusion.

2.2. Microphysics

In this article, we follow the burning scheme prescription proposed in Townsley et al. (2007). This improves the description of the chemical composition in the ash, which can be very different from the currently used seven-isotope network (including ^{4}He, ^{12}C, ^{16}O, ^{20}Ne, ^{24}Mg, ^{28}Si, and ^{56}Ni). We introduce the quantities $\bar{Y}$, $\bar{q}_B$, and ϕ_i ($i = 1, 2, 3$). They represent the inverse of the mean atomic mass ($1/\bar{A}$), binding energy, and the burning progress variables, and they follow the fluid advection. Operator splitting is used to solve separately fluid advection and nuclear reactions within and behind the deflagration wave. In the hydrodynamical phase, we solve the left-hand side of the below equations without the source terms, including

$$\frac{\partial \bar{Y}}{\partial t} + \boldsymbol{v}\cdot\nabla\bar{Y} = \dot{\bar{Y}}, \tag{1}$$

$$\frac{\partial \bar{q}_B}{\partial t} + \boldsymbol{v}\cdot\nabla\bar{q}_B = \dot{\bar{q}}_B. \tag{2}$$

After each step, the mean atomic mass $\bar{A}$ and mean atomic number $\bar{Z}$ are reconstructed by $1/\bar{Y}$ and $Y_{\rm e}/\bar{Y}$. $\bar{A}$ and $\bar{Z}$ are passed to the equation of state subroutine for finding other thermodynamics quantities including the pressure and its derivatives with respect to the local density and temperature.

After the hydrodynamical substep, we solve the nuclear burning phase. ϕ_1, ϕ_2, and ϕ_3 represent the burning of ^{20}Ne, burning until nuclear quasi-statistical equilibrium (NQSE) and that from NQSE to NSE. The level-set method is used for controlling the energy release by ϕ_1. To prevent burnt matter from repeatedly releasing energy due to numerical diffusion, ϕ_1, ϕ_2, and ϕ_3 are restricted to be monotonically increasing and ϕ_2 (ϕ_3) is allowed to evolve only when the burning represented by ϕ_1 (ϕ_2) is completely finished. Their evolution also satisfies the following equation

$$\frac{\partial \phi_i}{\partial t} + \boldsymbol{v}\cdot\nabla\phi_i = \dot{\phi}_i, \tag{3}$$

where $i = 1, 2, 3$. We also apply the operator splitting between the advection term and the source term. The source term is solved analytically. We remark that when the fluid elements are not in NSE, no electron capture takes place. This is a good approximation because the electron-capture rates below 5×10^9 K are in general much slower than the hydrodynamical timescale.

2.3. NSE and Weak Interactions

To couple the hydrodynamics with an extended nuclear reaction network for matter with a low $Y_{\rm e}$ matter typical in an ECSN, we prepare the NSE composition by the 495-isotope network with isotopes from ^{1}H to ^{91}Tc, (Timmes 1999) as a function of density ρ, temperature T, and $Y_{\rm e}$. The network also includes the Coulomb correction factor (Kitamura 2000). Matter with a temperature above 5×10^9 K is assumed to be in the NSE. We require the new composition $X_{\rm new}$, the new temperature $T_{\rm new}$, and the new specific internal energy $\epsilon_{\rm new}$ satisfying

$$\frac{\epsilon_{\rm new} - \epsilon}{\Delta t} = N_A(m_n - m_p - m_e)\frac{\Delta Y_{\rm e}}{\Delta t} + \dot{q}_\nu + \frac{q_B(X_{\rm NSE,new}) - q_B(X_{\rm NSE})}{\Delta t}. \tag{4}$$

We remind the reader that the composition in NSE is a function of density, temperature, and $Y_{\rm e}$ that $X_{\rm NSE,new} = X_{\rm NSE}(\rho_{\rm new}, T_{\rm new}, Y_{\rm e,new})$. The source terms on the right-hand side are the change of the binding energy when the composition changes, the energy loss due to neutron–proton mass difference and the energy loss by neutrino emissions during electron captures.

To obtain the electron-capture rates at low $Y_{\rm e}$, we follow Seitenzahl et al. (2010) and Jones et al. (2016) and extend the electron-capture rate table by including neutron-rich isotopes. Individual electron-capture rates given in Langanke & Martinez-Pinedo (2001) and Nabi & Klapdor-Kleingrothaus (1999) are used. We solve

$$\frac{dY_{\rm e}}{dt} = \sum_i X_i \frac{m_B}{m_i}(\lambda_i^{\rm ec} + \lambda_i^{\rm pc} + \lambda_i^{\rm bd} + \lambda_i^{\rm pd}), \tag{5}$$

where m_B and m_i are the baryon mass and the mass of the isotope i. $\lambda_i^{\rm ec}$, $\lambda_i^{\rm pc}$, $\lambda_i^{\rm bd}$, and $\lambda_i^{\rm pd}$ are the rates of electron capture, positron capture, beta-decay, and positron-decay by the isotope i, respectively, in units of s^{-1}.

3. Models and Results

3.1. Initial Model

In this section, we describe how we prepare the initial models for the hydrodynamical run. Each ONeMg core is modeled by the two-layer structure presented in Schwab et al. (2015). We obtain the necessary data (temperature, $Y_{\rm e}$ and composition) by extracting the numerical values from Figure 5 in their work. The inner part imitates the zone where electron captures take place. It has a lower $Y_{\rm e}$ and higher temperature in the inner part and vice verse for the outer part. The inner part has $(Y_{\rm e}, T) = (0.496, 4 \times 10^8\ {\rm K})$ and the outer part has $(Y_{\rm e}, T) = (0.5, 3 \times 10^8\ {\rm K})$. We assume that the chemical composition variation is small enough that it remains $X(^{16}{\rm O}) = 0.55$ and $X(^{20}{\rm Ne}) = 0.45$ throughout the star for simplicity. To maintain a high level of hydrostatic equilibrium, we do not map the initial model directly from the stellar evolutionary model, instead, we build the initial model by solving the equations for hydrostatic equilibrium using the given temperature and $Y_{\rm e}$ profiles in the mass coordinate. In Figure 1, we plot the initial density, temperature, $Y_{\rm e}$ and abundance profiles for model c3-09950-N.

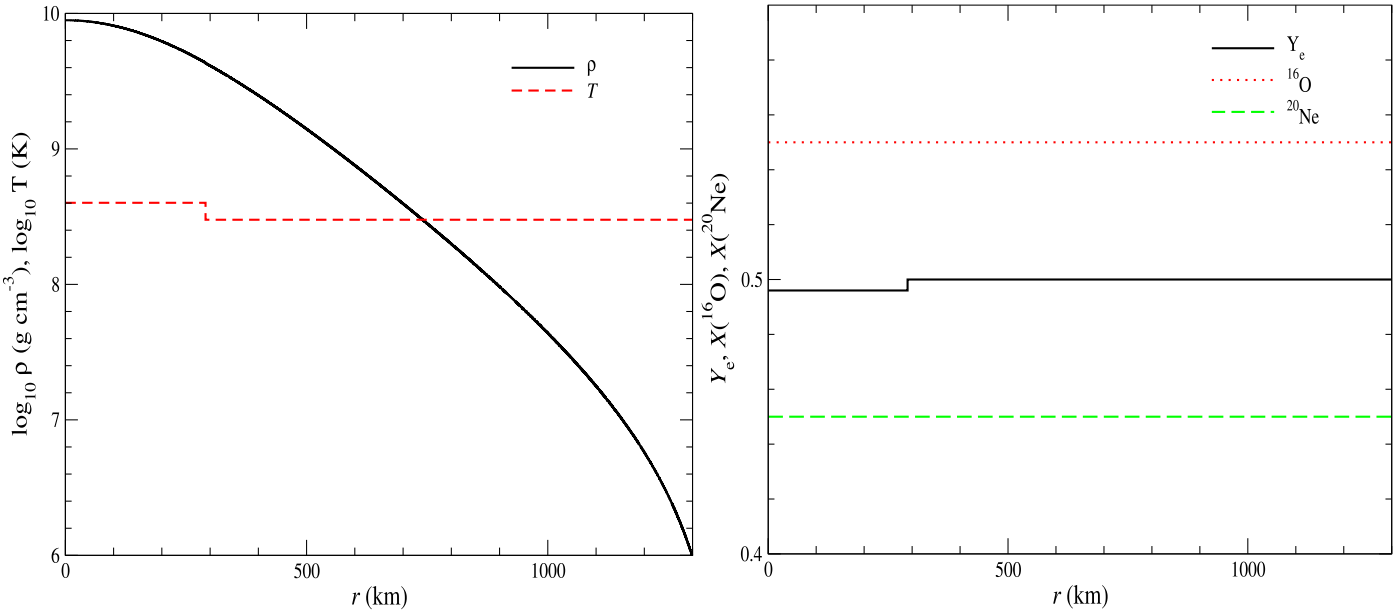

Figure 1. (Left panel) Initial density and temperature profiles of model c3-09950-N. (Right panel) Same as the left panel, but for the Y_e and abundances of major isotopes.

3.2. Numerical Models

3.2.1. Uncertainties in Stellar Evolutionary Models

The uncertainties in the evolution of an ONeMg core lead to the ambiguity of the ECSN evolution. The first one is the convection triggered by electron captures and O-burning before nuclear runaway takes place. Depending on the efficiency of core convection after O-burning has started, the ONe deflagration density in the ONeMg core increases from $\sim 10^{9.95}$ (Ledoux criterion) to $\sim 10^{10.2}\,\mathrm{g\,cm^{-3}}$ (Schwarzschild criterion). More efficient mixing leads to a higher central density (Takahashi et al. 2013). Note that even for the Ledoux criterion, hydrostatic O-burning forms a convectively unstable region, and thus the exact deflagration density depends on the competition between the heat generated by O-burning and the heat transport by convection. Therefore, $10^{9.95}\,\mathrm{g\,cm^{-3}}$ is the lower limit to the deflagration density. The exact density depends on the competition between the heat generation by the hydrostatic O-burning and the heat transport by the core convection.

The second uncertainty is the initial flame structure. The development of the initial flame is sensitive to the internal turbulent and convective motion of the star. In stellar evolution, which assumes spherical symmetry, the non-radial motion of matter is not included. Local turbulence can create velocity and temperature fluctuations, which are important to trigger the nuclear runaway. Efficient convection may smooth out the temperature fluctuations in the core and promote centered burning. The initial flame in the ONeMg core, similar to SNe Ia, cannot be constrained without the pre-supernova convective structure.

The third uncertainty is the relativistic correction of gravity. The impact of such correction is unclear. In an ONeMg core, the density in the core is sufficiently high that the electrons are ultra-relativistic. The contribution of the pressure and internal energy as a gravity source can be non-negligible. We want to understand how such corrections affect the dynamics, and whether the collapse criteria change with them.

The fourth uncertainty is how turbulence couples with flame propagation. The turbulent flame formalism assumes that the effective flame propagation speed is a function of velocity fluctuations from eddy motion. However, no experimental data is available for flame at such high Reynolds number $\mathrm{Re} \sim 10^{14}$. There are limited experiments using the terrestrial flame. In the literature of SNe Ia, theoretical arguments based on self-similarity (see, e.g., Pocheau 1994; Hicks 2015) are often used. The asymptotic velocity of turbulent flame remains unclear.

3.2.2. Model Description

The model parameters spanned in this work attempt to overlap the uncertainties in the stellar evolution modeling. In Table 2, we tabulate the initial setting of our hydrodynamical models. The initial models are built by referring to the pre-deflagration model computed in Schwab et al. (2015). In their models, the pre-deflagration ONeMg core consists of three parts, 1. the outer envelope where no burning occurs, 2. the outer core where hydrostatic burning of ^{24}Mg takes place, and 3. the inner core where electron capture and faster nuclear reactions occur.[4] We use the temperature and Y_e profiles to construct our initial models at different initial central densities. However, we do not resolve the innermost core around $10^{-4}\,M_\odot$, which is equivalent to less than a few grid points in our simulations.

The initial flame configuration is where vigorous hydrostatic O-burning takes place. We remind the reader that the precise geometry of the initial deflagration requires full multidimensional simulations right after the first nuclear runaway has started. We therefore implemented different flame structures to mimic different possible scenarios. In particular, we include the *c*3,

[4] We remark that some of the features in the stellar evolutionary models are omitted for numerical flexibility. The details of some minor elements such as ^{24}Mg are ignored. We do that because the flame burning algorithm does not fully distinguish the ^{24}Mg, which appears in the original fuel and in the ash after ^{20}Ne is first burnt. To completely avoid doubly releasing energy from the burning of ^{24}Mg, we decided to set the remaining ^{24}Mg abundance into ^{16}O, as both isotopes are burnt later than ^{20}Ne. Also, as we will show in coming sections, the distribution of Y_e plays a more important role to the evolution of the ONe WD. In general, such an approach might overestimate the energy production of the flame. In Section 3.8, we further study how the initial composition affects the collapse-explode bifurcation. Future works with more extensive on-site nuclear reaction network will be essential to distinguish this degeneracy.

Table 2
The Initial Configurations and the Final Results of the Simulations

Model	$\log_{10}\rho_c$	Flame	$Y_{e,\rm in}$	$Y_{e,\rm out}$	M	R	$Y_{e,\rm min}$	$t_{\rm coll}$	$M_{\rm burn}$	$E_{\rm tot}$	$E_{\rm nuc}$	Gravity	Results
c3-09800-N	9.80	*c*3	0.496	0.5	1.38	1.54	0.397	N/A	1.12	−0.16	8.19	N	E
c3-09850-N	9.85	*c*3	0.496	0.5	1.38	1.49	0.387	N/A	1.21	0.23	9.67	N	E
c3-09900-N	9.90	*c*3	0.496	0.5	1.39	1.45	0.357	0.96	1.00	N/A	7.92	N	C
c3-09900-R	9.90	*c*3	0.496	0.5	1.39	1.45	0.357	0.96	1.00	N/A	8.68	R	C
c3-09925-N	9.925	*c*3	0.496	0.5	1.39	1.42	0.354	0.76	0.52	N/A	6.83	N	C
c3-09950-N	9.95	*c*3	0.496	0.5	1.39	1.40	0.353	0.69	0.40	N/A	6.83	N	C
c3-09975-N	9.975	*c*3	0.496	0.5	1.39	1.38	0.353	0.63	0.34	N/A	6.70	N	C
c3-10000-N	10.0	*c*3	0.496	0.5	1.39	1.36	0.353	0.59	0.30	N/A	6.56	N	C
c3-10000-R	10.0	*c*3	0.496	0.5	1.39	1.36	0.353	0.59	0.30	N/A	6.56	R	C
c3-10200-N	10.2	*c*3	0.496	0.5	1.39	1.19	0.351	0.37	0.18	N/A	4.78	N	C
c3-10200-R	10.2	*c*3	0.496	0.5	1.39	1.19	0.351	0.37	0.18	N/A	4.78	R	C
b1a-09875-N	9.875	*b*1*a*	0.496	0.5	1.38	1.47	0.395	N/A	1.20	0.25	10.18	N	E
b1a-09900-N	9.90	*b*1*a*	0.496	0.5	1.39	1.45	0.382	N/A	1.32	0.26	12.39	N	E
b1a-09900-R	9.90	*b*1*a*	0.496	0.5	1.39	1.45	0.358	N/A	1.28	0.39	11.94	R	E
b1a-09925-N	9.925	*b*1*a*	0.496	0.5	1.39	1.42	0.364	0.73	0.68	N/A	6.21	N	C
b1a-09950-N	9.95	*b*1*a*	0.496	0.5	1.39	1.40	0.363	0.62	0.48	N/A	5.47	N	C
b1a-10000-N	10.0	*b*1*a*	0.496	0.5	1.39	1.36	0.360	0.51	0.34	N/A	4.37	N	C
b1b-09900-N	9.90	*b*1*b*	0.496	0.5	1.39	1.45	0.395	N/A	1.17	0.13	9.91	N	E
b1b-09950-N	9.95	*b*1*b*	0.496	0.5	1.39	1.40	0.388	N/A	1.37	0.27	13.47	N	E
b1b-09975-N	9.975	*b*1*b*	0.496	0.5	1.39	1.38	0.364	0.58	0.74	N/A	6.98	N	C
b1b-10000-N	10.0	*b*1*b*	0.496	0.5	1.39	1.36	0.357	0.49	0.54	N/A	5.94	N	C
mc3-09850-N	9.85	*mc*3	0.496	0.5	1.38	1.49	0.395	N/A	1.10	0.23	9.17	N	E
mc3-09900-N	9.90	*mc*3	0.496	0.5	1.39	1.45	0.375	N/A	1.36	−0.37	10.07	N	E
mc3-09925-N	9.925	*mc*3	0.496	0.5	1.39	1.42	0.355	0.64	0.53	N/A	5.86	N	C
mc3-09950-N	9.95	*mc*3	0.496	0.5	1.39	1.40	0.355	0.56	0.40	N/A	5.06	N	C
bc3-09925-N	9.925	*bc*3	0.496	0.5	1.39	1.42	0.395	N/A	1.14	0.13	10.12	N	E
bc3-09950-N	9.95	*bc*3	0.496	0.5	1.39	1.40	0.386	N/A	1.26	0.48	12.12	N	E
bc3-09975-N	9.975	*bc*3	0.496	0.5	1.39	1.38	0.354	0.54	0.73	N/A	6.94	N	C
b1b-09950-N-Lam	9.95	*b*1*b*	0.496	0.5	1.39	1.40	0.375	1.15	0.02	N/A	0.07	N	C
b1b-09975-N-Lam	9.975	*b*1*b*	0.496	0.5	1.39	1.38	0.377	1.34	0.04	N/A	0.88	N	C
b1b-10000-N-Lam	10.0	*b*1*b*	0.496	0.5	1.39	1.36	0.374	0.97	0.02	N/A	0.16	N	C
bc3-09950-N-vf025	9.95	*bc*3	0.496	0.5	1.39	1.40	0.368	0.55	0.07	N/A	2.42	N	C
bc3-09950-N-vf050	9.95	*bc*3	0.496	0.5	1.39	1.40	0.368	0.56	0.71	N/A	5.74	N	C
bc3-09950-N	9.95	*bc*3	0.496	0.5	1.39	1.40	0.386	N/A	1.26	0.48	12.12	N	E
bc3-09950-N-B025	9.95	*bc*3	0.496	0.5	1.39	1.40	0.365	0.61	0.51	N/A	4.83	N	C
bc3-09950-N-B050	9.95	*bc*3	0.496	0.5	1.39	1.40	0.367	0.55	0.53	N/A	5.14	N	C
bc3-09950-N-B075	9.95	*bc*3	0.496	0.5	1.39	1.40	0.367	0.54	0.70	N/A	6.28	N	C
bc3-09950-N	9.95	*bc*3	0.496	0.5	1.39	1.40	0.386	N/A	1.26	0.48	12.12	N	E

Note. $\log_{10}\rho_c$ is the logarithmic of the initial central density in units of g cm^{-1}. $Y_{e,\rm in}$ and $Y_{e,\rm out}$ are the initial electron fraction of the core and envelope. $Y_{e,\rm min}$ is the minimum electron fraction reached in the simulation. $t_{\rm coll}$ is the time-lapse from the beginning of simulation to the moment where the central density exceeds 10^{11} g cm^{-1}. No $t_{\rm coll}$ is given for models that expand. M and $M_{\rm burn}$ are the initial mass and the amount of matter burnt by deflagration in units of $M_\odot$. R is the initial radius of the star in units of 10^3 km. $E_{\rm tot}$ and $E_{\rm nuc}$ are the final energy and the energy released by nuclear reactions in units of 10^{50} erg. $E_{\rm tot}$ is not recorded for models that collapse. "Gravity" means the choice of gravity source term assuming Newtonian ("N") and with relativistic corrections ("R"). "Results" stand for the final fate of the ONeMg core, where "C" ("E") means that the core collapses (expands) when the simulation is stopped.

*b*1*a*, *b*1*b*, and *b*5 flame structures (see Figure 2 of Reinecke et al. 1999 for graphical illustrations). The *c*3 flame is the same "three-finger" structure as in Niemeyer et al. (1995). The "finger shape" can enhance the development of Rayleigh–Taylor instabilities. Also, this shape prevents the development of enhanced flow along the boundary, which might not be physical. A *c*3 flame includes an outer radius of ∼40 km and an inner radius of 20 km. The flame structure is similar to what we have used to trigger the deflagration phase in Leung et al. (2015a, 2015b) but with a smaller size. The *b*1*a* flame assumes a bubble of radius 15 km located at 50 km away from the center. In general, the exact position of the initial flame depends on competition between heating by nuclear reactions and energy transport by convection. For an ONeMg core, it is determined by whether the hydrostatic O-burning takes place in the center or off-center, and whether it triggers convection during burning. However, the exact details remain less understood because of numerical difficulties in the stellar evolution of the ONeMg core before nuclear runaway. In Figure 2, we plot the temperature color plot to show the initial flame structure *c*3, *b*1*a*, and *b*1*b*, respectively. We also include variations of the *c*3 flame by changing its size to achieve different initial burnt masses $M_{\rm burn,ini}$. This attempts to overcome the uncertainties in the unresolved region during the final hydrostatic oxygen burning before the onset of thermonuclear runaway.

We also do not keep the details of the innermost part (∼10–20 km) in the initial model because there is competition between the very late-phase electron captures during off-center O-burning and its related convective mixing. The exact $Y_{\rm e}$ profile in that region is unclear. The question is further complicated by the initial flame. Despite that, they correspond to a few grids in

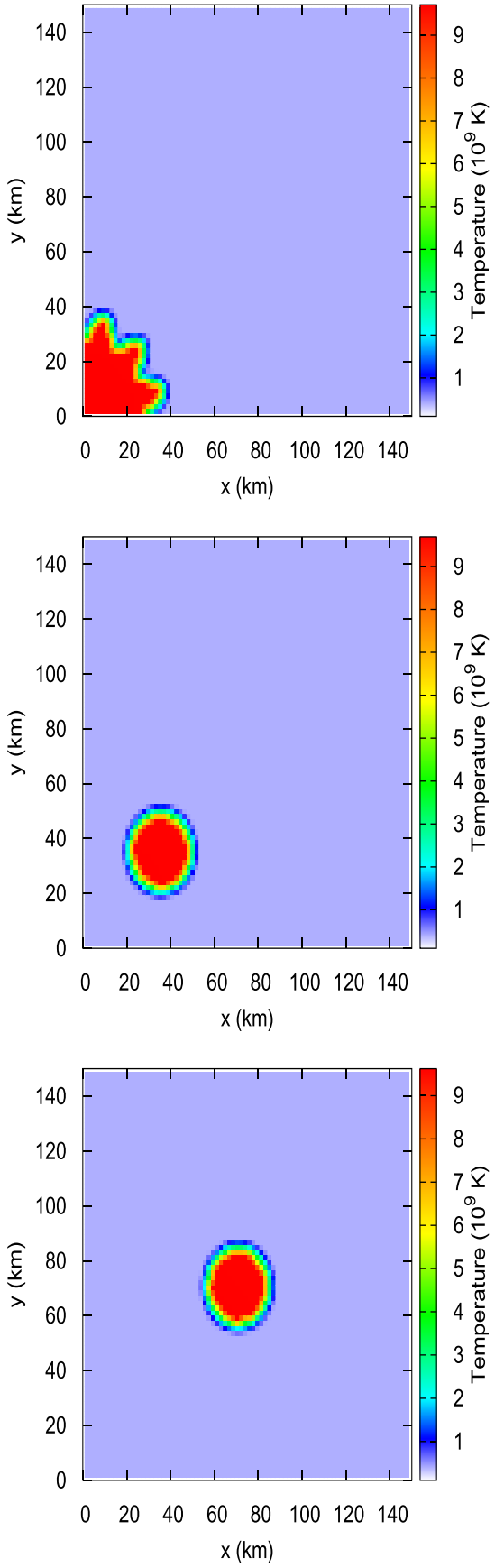

Figure 2. (Top panel) Temperature color plot for the initial flame profile *c*3 using model c3-09950-N. (Middle panel) Same as the top panel, but for the initial flame profile *b*1*a*. (Bottom panel) Same as the top panel, but for the initial flame profile *b*1*b*.

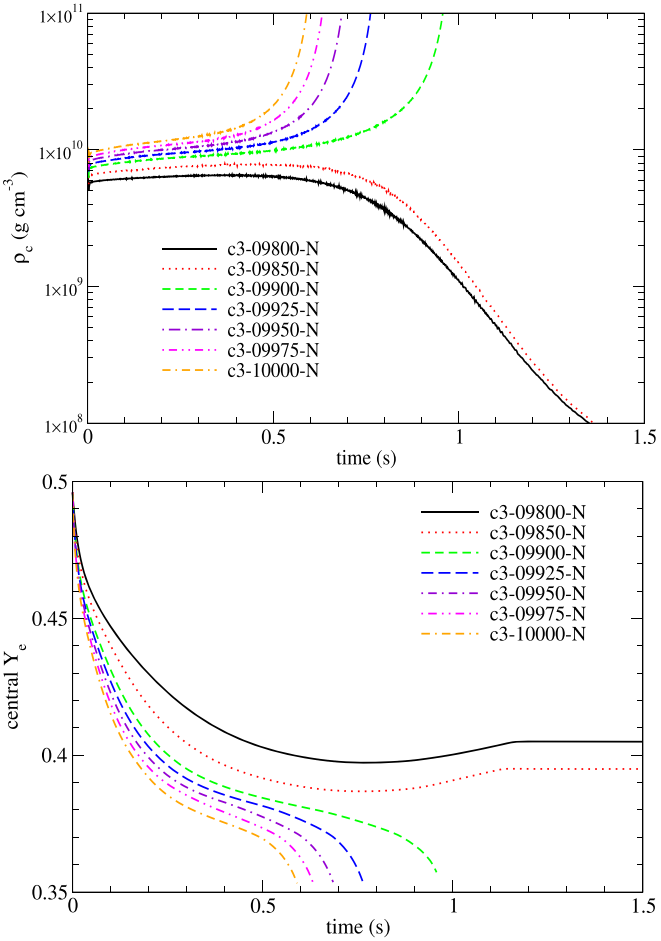

Figure 3. (Top panel) Time evolution of the central densities of models c3-09800-N ($\rho_c = 10^{9.8}$ g cm^{-3}), c3-09850-N ($\rho_c = 10^{9.85}$ g cm^{-3}), c3-09900-N ($\rho_c = 10^{9.9}$ g cm^{-3}), c3-09925-N ($\rho_c = 10^{9.925}$ g cm^{-3}), c3-09950-N ($\rho_c = 10^{9.95}$ g cm^{-3}), c3-09975-N ($\rho_c = 10^{9.75}$ g cm^{-3}), and c3-10000-N ($\rho_c = 10^{10}$ g cm^{-3}). All models assume Newtonian gravity and the initial flame geometry *c*3. Refer to Table 2 for details of the configurations. (Bottom panel) The evolution of central Y_e for the same models shown in the upper panel, which compares the effects of the initial central density (also the initial mass) on the final evolution.

the simulation box. In this work, we assume a flat Y_e profile in the core and patch the flame directly on the initial model. The effect of the initial Y_e profile can be refereed from Section 3.7.

3.3. Effects of Central Density

3.3.1. Model with a Centered Ignition Kernel

In this section, we discuss the global behavior of the ONeMg cores with different initial central densities and a centered flame at the beginning of simulations.

In all of our simulations, we follow the evolution of each model until the central density ρ_c reaches 10^{11} g cm^{-3} (collapse case) or when the total time reaches 1.5 s (expansion case). For models with a heading of *c*3 (models c3-09800-N, c3-09850-N, c3-09900-N, c3-09925-N, c3-09950-N, c3-09975-N, c3-10000-N), we compute the deflagration phase of the ONeMg core at different initial central densities but with the same flame structure of *c*3 using the Newtonian gravity. (We postpone the comparison of flame development in Section 3.6.1.) In this series of models, when the initial central density increases, the total mass increases from 1.38 to 1.39 $M_\odot$. Only a mild rise in

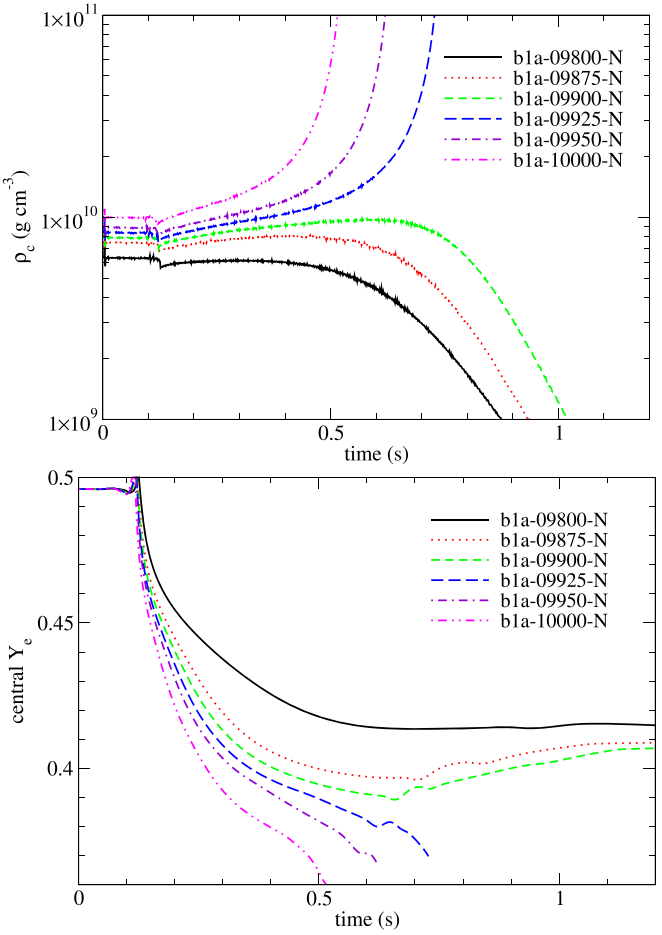

Figure 4. (Top panel) Time evolution of the central densities of models b1a-09875-N ($\rho_c = 10^{9.875}$ g cm^{-3}), b1a-09900-N ($\rho_c = 10^{9.9}$ g cm^{-3}), b1a-09925-N ($\rho_c = 10^{9.925}$ g cm^{-3}), b1a-09950-N ($\rho_c = 10^{9.95}$ g cm^{-3}) and b1a-10000-N ($\rho_c = 10^{10.0}$ g cm^{-3}). The models share the same setting of Newtonian gravity and the initial flame geometry *b1a*. (Bottom panel) The central Y_e evolution for the the same set of models shown in the upper panel.

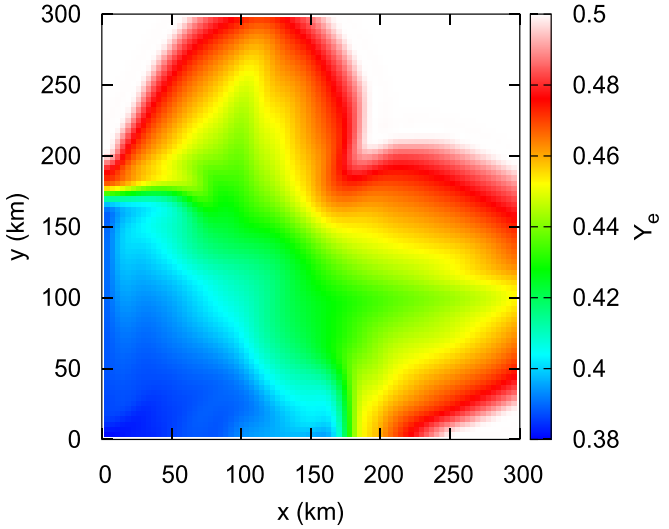

Figure 5. The Y_e distribution of model b1a-09925-N at $t = 0.625$ s. The aspherical distribution distribution of Y_e can produce bumps in the evolution of Y_e.

mass is observed because of the highly relativistic and degenerate electron gas. On the other hand, the radius decreases from 1.54×10^3 to 1.36×10^3 km, showing that the ONeMg core is becoming more compact as the central density increases. The minimum Y_e also drops when ρ_c increases, because the typical electron-capture rate increases when ρ_c increases for the same Y_e. The collapse time, which is related to how fast the Y_e drops, also decreases. Similarly, we observe a decrease in the burnt mass.

For models that expand, i.e., models c3-09800-N and c3-09850-N, $\sim 1\,M_\odot$ is burnt. In the collapsing models, the faster they collapse, the smaller amount of fuel is burnt. The final energy ($\sim 10^{49}$ erg) is much lower than typical SNe Ia ($\sim 10^{50}$ erg).

In the upper panel of Figure 3, we plot the central densities for models c3-09800-N, c3-09850-N, c3-09900-N, c3-09925-N, c3-09950-N, c3-09975-N, and c3-10000-N. In all models, the central densities increase in the first 0.5–0.7 s where the electron captures dominate the dynamics. Models with a central density greater than $10^{9.9}$ g cm^{-3} collapse directly within 0.5–1.0 s, where the contraction rate increases with the central density. Models with a lower initial central density expand after $\sim$0.6 s, showing that the energy released by the deflagration wave is sufficient to balance the loss of pressure after electron captures.

In the lower panel of Figure 3, we plot the central electron fraction (Y_e) as a function of time for the same models as the upper panel. Unlike the central densities, the central electron fraction drops drastically in the first 0.5 s, and then the decrease slows down. The equilibrium Y_e decreases while the initial central density increases. For the models that directly collapse, the drop of central Y_e slows down at $Y_e \approx 0.38$ around 0.3–0.5 s. Then, it further decreases to 0.36, as the central densities of these models further increase to 10^{11} g cm^{-3}. For models that expand, the central electron fraction drops similarly to the collapsing models, but they reach a higher intermediate Y_e compared to those models. In particular, models c3-09800-N and c3-09850-N show an equilibrium Y_e of 0.39 and 0.40, respectively, at $t \approx 0.7$–0.8 s after the deflagration has started. Following the expansion of the star, the central Y_e gradually increases and reaches the equilibrium value of $\sim$0.40 at $t \approx 1.1$ s.

3.3.2. *The* b1a *Series*

For models with a heading *b1a* (models b1a-09800-N, b1a-09875-N, b1a-09900-N, b1a-09925-N, b1a-09950-N, and b1a-10000-N), they are the ONeMg core models similar to those above, but with an initial flame *b1a*, which means a flame bubble (a ring in the three-dimensional projection) of a radius 15 km at 50 km away from the ONeMg core center. The initial models are the ONeMg cores in different initial central densities in hydrostatic equilibrium. The initial masses and radii are the same as those in the *c3* series. Models b1a-09800-N, b1a-09875-N, and b1a-09900-N are exploding while the others are collapsing. In general, the trends of Y_e at the end of the simulations are similar in that a higher initial central density implies a lower Y_e at the end of the simulations. However, for models with the initial same central density, Y_e is higher for the *b1a* flame than for the *c3* flame. Also, less mass is burnt, and the direct collapse occurs faster, for the same central density, with the exception of model b1a-09875-N. As there is a shorter time for the deflagration wave to sweep the fuel before the core collapse,

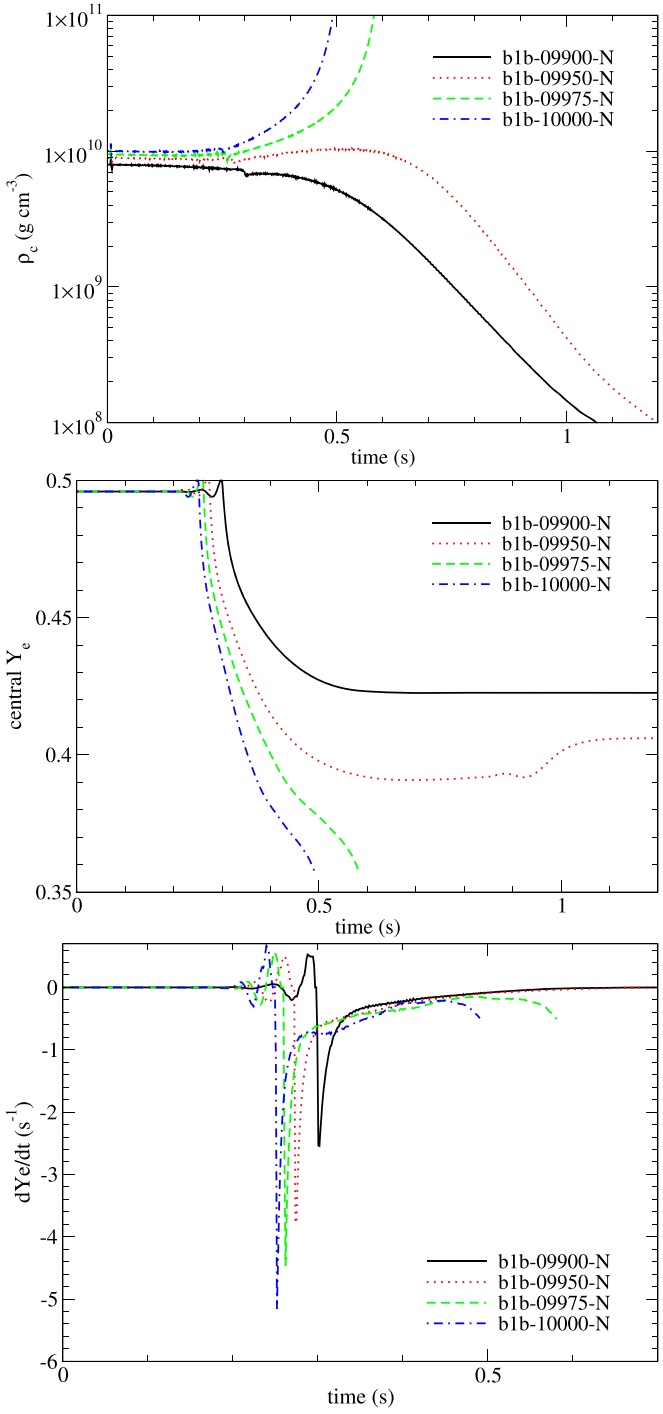

Figure 6. (Top panel) Time evolution of the central densities of models b1b-09900-N ($\rho_c = 10^{9.9}$ g cm^{-3}), b1b-09950-N ($\rho_c = 10^{9.95}$ g cm^{-3}), b1b-09975-N ($\rho_c = 10^{9.975}$ g cm^{-3}), and b1b-10000-N ($\rho_c = 10^{10.0}$ g cm^{-3}). All models assume Newtonian gravity and the initial flame geometry *b1b*. (Middle panel) Same as the upper panel, but for the evolution of the central Y_e for the same set of models. (Bottom panel) Time derivative of Y_e for the same set of models as in the upper panel.

less energy is released by nuclear reactions when the initial ρ_c increases. The general pattern for the *b1a* series is similar to that of the *c3* series.

In the upper panel of Figure 4 we plot the central density against time similar to Figure 3. Due to the off- center burning, there is no change in the central density before 0.1 s. Once the flame reaches the center, the central density drops rapidly due to the expansion of matter. After the initial expansion, the central density of all models increases. Models with an initial central density greater than $10^{9.925}$ g cm^{-3} reach the threshold density between 0.4 and 0.7 s. Again, the collapse time decreases when the central density increases. On the contrary, models b1a-09800-N, b1a-09875-N and b1a-09900-N expand at about 0.5–0.7 s. In particular, the central density of model b1a-09900-N can reach as high as 10^{10} g cm^{-3}, before the expansion takes place. Such a high central density can be observed for models near the bifurcation density, where the flame requires more time to grow until it can balance the electron-capture effects.

Similarly to the upper panel of Figure 4, in the lower panel we plot the central Y_e evolution of model b1a-10000-N. As with the central density, there is no change in central Y_e before 0.1 second, when the flame has not reached the core. After that, it quickly drops with a rate proportional to the central density and slows down after it reaches ∼0.38–0.41. For models that directly collapse, the central Y_e quickly falls rapidly again and reaches 0.35–0.36 at the end of the simulations. In models b1a-09925-N and b1a-09950-N, there are mild bumps in the central Y_e at $t \approx 0.6$ s. This is because the off-center burning has led to an uneven distribution of Y_e. Unlike the models with *c3* flame, the central ignition allows for the matter with a higher density to be burnt for a longer time, thus having more time for electron capture and a lower Y_e. This creates a distribution of increasing Y_e along the radial outward direction. For the *b1a* cases, the region that undergoes the longest duration of electron capture is away from the center. Furthermore, in the core, before the homologous expansion fully develops, mixing from neighboring cells may also affect the Y_e distribution. The temporary inward flow to the center can also increase the central Y_e. In Figure 5, we plot the Y_e distribution of model b1a-09925-N at $t = 0.625$ s. Near the center, Y_e is not completely spherically symmetric. Such asymmetry may give rise to small-scale bumps in the Y_e evolution. However, for model b1a-10000-N, the direct collapse occurs without reaching any intermediate Y_e. Therefore, the electron capture around all the regions is similar. Y_e only drops monotonically with time.

3.3.3. *The* b*1*b *Series*

In this series, we further study the density dependence of an ONeMg core with an off-center flame placed at 100 km from the stellar center. The models include models b1b-09900-N, b1b-09950-N, b1b-09975-N, and b1b-10000-N. The flame structure in this series of models is similar to *b1a*, but the flame "ring" is located at 100 km away from the core. Similarly to the *b1a* series, the initial profiles are the same as those of the *c3* series in that the models have the same masses and radii. In this series, models b1b-09900-N and b1b-09950-N are expanding while the others are directly collapsing. Similarly to the two series above, when the central density is higher, the final Y_e at the end of the simulation is lower, and the model has a faster collapse. Less nuclear energy is released, owing to a smaller mass of fuel burnt by the deflagration wave.

In the upper panel of Figure 6, we plot the central density against time for the four models, similar to Figures 3 and 4. With a flame bubble located farther from the center, the flame takes ∼0.3 s to reach the center, which creates a small drop in the central density. At ∼0.5 s, models b1b-09975-N and b1b-10000-N begin their collapse. The central density of model

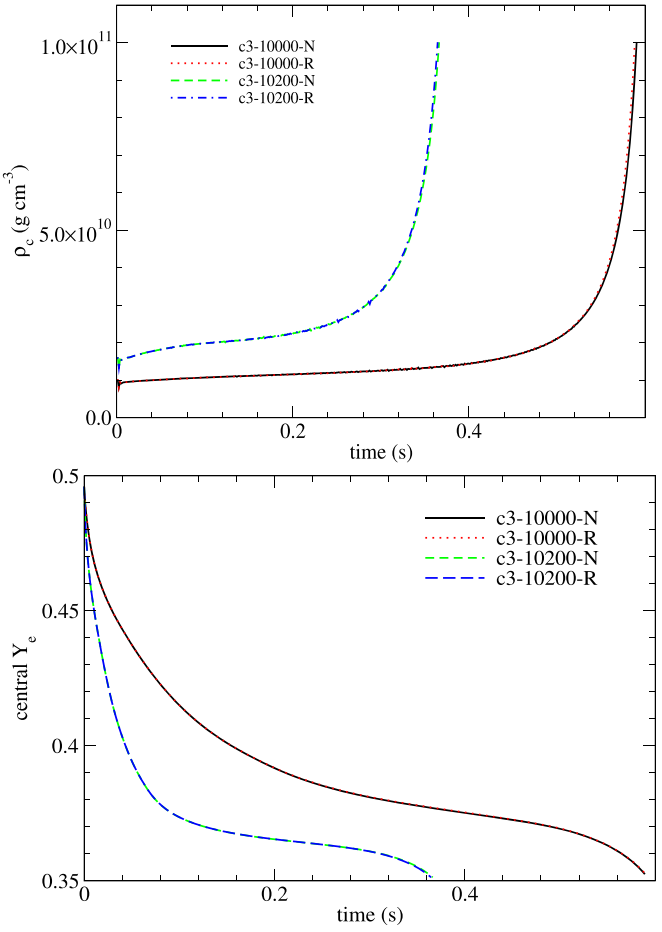

Figure 7. (Top panel) Central densities against time for models c3-10000-N ($\rho_c = 10^{10}$ g cm^{-3}, Newtonian gravity), c3-10000-R ($\rho_c = 10^{10}$ g cm^{-3}, with relativistic corrections), c3-10200-N ($\rho_c = 10^{10.2}$ g cm^{-3}, Newtonian gravity), and c3-10200-R ($\rho_c = 10^{10.2}$ g cm^{-3}, with relativistic corrections). (Bottom panel) Same as the upper panel, but for the central Y_e for the same set of models.

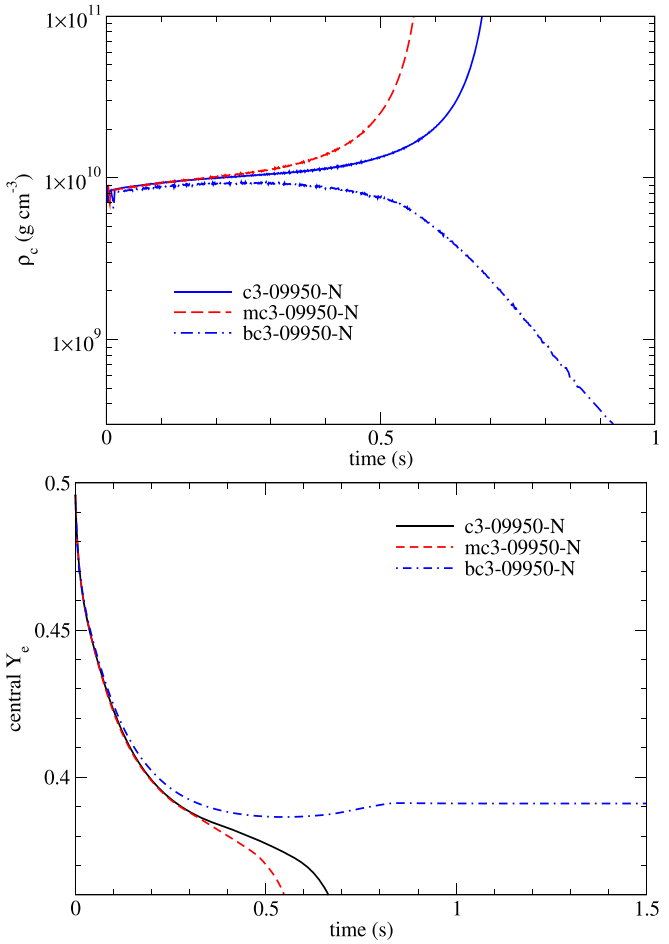

Figure 8. (Top panel) Time evolution of the central densities in models c3-09950-N (*c*3 initial flame), mc3-09950-N (*mc*3 initial flame), and bc3-09950-N (*bc*3 initial flame). All models share the same initial central density ($\rho_c = 10^{9.95}$ g cm^{-3}) and are without relativistic corrections. (Bottom panel) Same as the upper panel but for the central Y_e for the same set of models.

b1b-09950 also increases above 10^{10} g cm^{-3} at ∼0.5 s but drops again when the star expands at 0.7 s. Model b1b-09900 shows almost no contraction when the electron captures take place at the core. This is because the typical density is low and the initial flame is sufficiently far. The burnt matter can expand before the flame reaches the center.

In the middle panel of Figure 6, we plot the time evolution of the central Y_e for the same series of models as in the upper panel. There is no change in Y_e in the first 0.3 s. This is because the flame has not arrived at the core. Thus, the cold matter cannot carry out efficient electron captures compared to the burnt ash. After the deflagration wave has arrived at the center, Y_e drops immediately. When the initial ρ_c is higher, its rate of Y_e decrease is higher. In models b1b-09750-N and b1b-10000-N, the electron captures mildly slow down when $Y_e \approx 0.37$, and then the drop resumes again until the end of the simulations, down to a value of ≈0.36. In contrast, Y_e shows temporary values at 0.39 and 0.42 for models b1b-09900-N and b1b-09950-N. The value of the latter remains the same after the expansion has started, while the value of the former slightly increases to 0.41, as the matter in the core begins to mix with the surrounding material, which has a higher Y_e.

We also notice that at early time there is a mild drop in the central density before the flame arrives at the center. This is not because the model is not in good equilibrium during construction, but because the initial off-center flame and its subsequent electron captures disturb the pressure gradient. The core slowly expands to adjust to the presence of the flame.

In the bottom panel of Figure 6, we plot the time derivative of the central Y_e to illustrate the density dependence of the electron-capture rate. Depending on the central density, the arrival time of the deflagration wave differs by at most 0.05 s. Such a small time difference can provide the time for the deflagration wave to grow larger and, hence, burn more matter, which suppresses the contraction after the flame reaches the center. Once the center is burnt, the sharp drops of $dY_{e,c}/dt$ show that the weak interactions rapidly occur in the high-density core. Furthermore, the rate of decrease increases when the initial ρ_c increases. This shows that the rate of decreases is an increasing function of the progenitor mass, i.e., the initial runaway density.

3.4. Effects of General Relativity

Here, we study how the relativistic corrections in the gravity can affect the bifurcation of the ONeMg core evolution. In the simulations, we study the counterpart models of c3-10000-N and c3-10200-N, i.e., models c3-10000-R and c3-10200-R. These models are the most compact ONeMg cores constructed in this work; therefore, we expect that the relativistic effects in

these cores are the most pronounced. In general, embedding the physics of relativistic gravity requires a complete restructuring of the code due to the necessary inclusion of the metric tensor. We look for corrections of Newtonian gravity as the first step. We follow the prescription in Kim et al. (2012). Based on the Poisson equation for the gravitational potential $\nabla^2\Phi = 4\pi G\rho$, where Φ and ρ are the gravitational potential and matter mass density. We replace ρ by $\rho_{\rm active}$, where

$$\rho_{\rm active} = \rho h\frac{1+v^2}{1-v^2} + 2P, \quad (6)$$

and P and v^2 are the fluid pressure and the magnitude square of the velocity, respectively. $h = 1 + \epsilon + P/\rho$ is the specific enthalpy of the matter. In this sense, the extra mass-energy contributions by the internal energy and the kinematics of the matter are included.

To demonstrate the effects of the relativistic corrections in the gravitational potential, in the upper panel of Figure 7, we plot the central density for the models with a centered flame with an initial geometry $c3$ and initial central densities $10^{10.0}$ and $10^{10.2}$ g cm^{-3}, respectively. The lower panel of Figure 7 is the same as the upper panel but for the central $Y_{\rm e}$. In both cases, a direct collapse is observed. The evolution of the central density is not sensitive to the relativistic corrections in gravity. Models c3-10000-N and c3-10000-R overlap with each other in the figure throughout the simulation, as do models c3-10200-N and c3-10200-R. Similar results can be found for the central $Y_{\rm e}$.

By combining these models, we show that when GR correction terms in gravity are included, there is no observable change in the evolution even for the most compact models with the initial $\rho_c = 10^{10.2}$ g cm^{-3}. This suggests that Newtonian gravity is sufficient in following the runaway phase of an ONeMg core accurately before its onset of collapse.

3.5. Effects of Initial Flame Size

The exact extent of the nuclear runaway is not well constrained because it depends on the competition between the convective efficiency and the hydrostatic O-burning. Numerically, it is difficult to implement due to the sharp $Y_{\rm e}$ contrast and complications from the Urca process. In general, efficient convection leads to a faster transport of the heat produced during electron captures. This smooths the temperature profile, allows for a larger initial flame, and raises the ignition density accordingly.

Without knowing the exact details of the initial flame evolution, we try to span the parameter space by considering different flame sizes for the central ignition model. They include $c3$, $mc3$, and $bc3$. The latter two flame structures are the same as the $c3$ flame, but with a size two or four times larger. The width of the reaction front is kept fixed as indicated by the level-set scheme. The case $bc3$ is so extended that it might be incompatible with typical stellar evolution. We use it as a qualitative comparison in this work.

In the upper panel of Figure 8, we plot the evolution of central densities against time for models of different initial flame masses. The initial mass being burnt $M_{\rm burn,ini}$ ranges from 10^{-4} to $10^{-2}\,M_\odot$. For model c3-09950-N with $M_{\rm burn,ini} \sim 10^{-4}\,M_\odot$, the central density increases for the first 0.1 s. The models deviate at $\sim$0.3 s. Beyond $t = 0.7$ s, the ONeMg core collapses. On the other hand, when $M_{\rm burn,ini} \sim 10^{-3}\,M_\odot$, a similar evolution occurs but the collapse starts earlier, at 0.5 s after the simulation. When

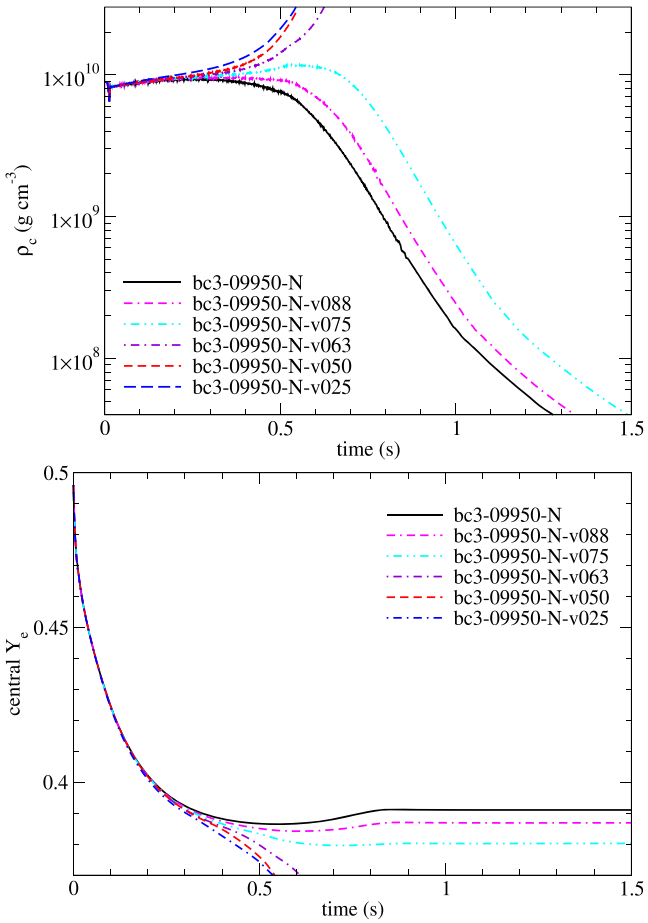

Figure 9. (Top panel) Time evolution of central densities against time for models bc3-09950-N ($C_n = C_{n0}$), bc3-09950-N-vf050 ($C_n = 0.5\,C_{n0}$), and bc3-09950-N-vf025 ($C_n = 0.25\,C_{n0}$). Extra models are plotted including models bc3-09950-N-vf063 ($C_n = 0.63\,C_{n0}$), bc3-09950-N-vf075 ($C_n = 0.75\,C_{n0}$), and bc3-09950-N-vf088 ($C_n = 0.88\,C_{n0}$). All models share the same initial flame geometry $bc3$, central density of $10^{9.95}$ g cm^{-3} and assume Newtonian gravity. (Bottom panel) Same as the upper panel but for the central $Y_{\rm e}$ for the same set of models. For the expanding models (bc3-09950-N, bc3-09950-N-vf088, and bc3-09950-N-vf075), the flame speed affects final $Y_{\rm e}$.

$M_{\rm burn,ini} \sim 10^{-2}\,M_\odot$, a similar contraction occurs at the beginning, but after $t = 0.5$ s, the star's central density decreases due to expansion of the ONeMg core. It produces a low-energy supernova explosion, similar to a "Type 1.5x" supernova (when a realistic progenitor model including an H-envelope is considered).

The lower panel of Figure 8 is the same as the upper panel but for the central $Y_{\rm e}$. Similarly to previous models, all three models show a rapid drop of the central $Y_{\rm e}$ once the core is burnt to NSE. It drops to about 0.39 within 0.3 s, until the capture rate decreases. The equilibrium $Y_{\rm e}$ of c3-09950-N is slightly higher than that in models mc3-09950-N and bc3-09950-N. At $t = 0.5$–0.6 s, $Y_{\rm e}$ drops rapidly again for models c3-09950-N and mc3-09950-N. However, in model c3-09950-N, due to expansion, mixing occurs in the core with the matter in the outer zones, which has, on average, a higher $Y_{\rm e}$. The $Y_{\rm e}$ slowly increases to 0.39 and remains unchanged after $t = 0.8$ s.

These figures show that the initial flame size also plays a role in determining the collapse-expansion bifurcation. In particular, a small flame $\sim 10^{-4}$–$10^{-3}\,M_\odot$ favors the collapse scenario, while a large flame favors the expansion scenario. In Section 4,

we further discuss the non-monotonic variations of the collapse time among models with the *c*3, *mc*3, and *bc*3 flame structures.

3.6. Effects of Flame Physics

In order to model a turbulent flame, a formula describing the relation between the turbulent velocity v' and the effective flame propagation speed $v_{\rm turb}$ is necessary. However, only a statistical description is available due to the stochastic nature of turbulent motion. Also, a terrestrial experiment cannot create such an extreme environment. How the turbulent motion can enhance the propagation of flame and also the effective flame speed remains unclear. In the literature of SN Ia where turbulent flame models are used, the models assume self-similar flames. With the renormalization scheme (Pocheau 1994), the general formula writes

$$v_{\rm turb} = v_{\rm lam}\left[1 + C_n\left(\frac{v'}{v_{\rm lam}}\right)^n\right]^{1/n}, \quad (7)$$

where $v_{\rm lam}$ is the laminar flame propagation speed, while C_n and n are the constants derived from experiments. The velocity spectra of the turbulence structure determine n. This formula has two asymptotic properties that are expected experimentally: (1) The effective propagation speed reduces to the laminar flame speed, when $v' \to 0$. This corresponds to the case that, when there is no perturbation to the surface structure of the flame, the flame propagates as a laminar wave; and (2) the effective propagation speed has an asymptotic value $\approx \sqrt[n]{C_n}\, v'$ (Given $v' > v_{\rm lam}$). This means that when the fluid motion is highly turbulent, the flame no longer depends on the laminar flame speed but solely on the velocity fluctuations inside the fluid.

However, one shortcoming of this model is that in order to derive this formula, isotropic turbulence is assumed by the renormalization procedure. Gravity makes the radial direction distinctive from the angular directions. Furthermore, the Rayleigh–Taylor instabilities enhance the flame propagation along the radial direction.

Numerically, one has different C_n and n based on the context. In Peter (1999) and Schmidt et al. (2006), $C_n = 4/3$ and $n = 2$ correspond to the Gaussian distribution in the velocity fluctuations. In Hicks (2015), it is shown numerically that for a premixed flame with a one-way reaction such as H_2-air mixture, the relation has a best fit of $C_n = 0.614$ when $n = 2$, while $v_{\rm turb} = v_{\rm lam}(1 + 0.4321\tilde{v}'^{1.997})$ is the best fit, where $\tilde{v}'$ is the scaled v'. The variations of this formula demonstrate that the scaling factor C_n and the scaling power n are not yet well constrained.

To understand the effects of this quantity on the ONeMg core evolution, we vary the original value of C_n (denoted as C_{n0}) by considering $C_n = 0.25\, C_{n0}$ and $0.50\, C_{n0}$. They correspond to the turbulent flame where turbulent production is less effective in disturbing the flame structure.

In the upper panel of Figure 9, we plot the central density against time for models bc3-09950-N, bc3-09950-vf050, and bc3-09950-vf025. We choose the basis model with the *bc*3 flame structure because it has a bifurcation density near $10^{9.95}$ g cm^{-3}. The effects of the flame physics are more pronounced near the bifurcation density. We note that in our models, the transition density for the *c*3 flame is $\sim 10^{9.90}$ g cm^{-3}, and using a slower flame does not change the fate of the model at $10^{9.95}$ g cm^{-3} from its collapse into a neutron star. Thus, we consider the *bc*3 flame, where the transition occurs at a central density of $10^{9.95}$ g cm^{-3}. In fact, similar effects can also be demonstrated by the ONeMg models with the *c*3 flame and a central density near $10^{9.90}$ g cm^{-3}. In this series of models, model bc3-09950-N explodes while models bc3-09950-vf050 and bc3-09950-vf025 collapse. We also plot the results from additional models (not included in Table 2) for demonstrating the sensitivity of our models on the flame speed by including models bc3-09950-N-vf063, bc3-09950-N-vf075, and bc3-09950-N-vf088, which are 63%, 75%, and 88% of the default asymptotic flame speed.

The central density of all models mildly increase for the first 0.3 s. For the collapsing models, the increase of ρ_c resumes at $t \approx 0.4$ s. On the other hand, for the expanding models, such as model bc3-09950-N, ρ_c slowly drops until $t = 0.6$ s. Accompanying with the expansion, its central density rapidly drops after $t = 0.6$ s. At $t = 1$ s, the central density drops to about 1% of its initial value. When the flame speed is high, the conversion from contraction to expansion becomes fast and so is the expansion of the core.

In the lower panel of Figure 9, we plot the central $Y_{\rm e}$ similar to Figure 9. In the exploding model bc3-09950-N, the central $Y_{\rm e}$ again quickly drops from 0.5 to 0.38 within 0.3 s. Unlike the previous test on the effects of the initial flame size, the large initial flame we used is less changed by its surroundings. Beyond $t = 0.3$ s, the drop of $Y_{\rm e}$ accelerates again and the central $Y_{\rm e}$ drops below 0.37 at $t = 0.5$ s. On the other hand, for the models that expand, during their expansion, the central $Y_{\rm e}$ drops until it reaches its asymptotic value 0.38–0.39 after $t = 0.8$ s. We remark that the asymptotic $Y_{\rm e}$ increases when the flame speed is faster. Notice that the final $Y_{\rm e}$ determines the characteristic abundance of the ash, especially when it is ejected. The low-$Y_{\rm e}$ ejecta contains a significant overproduction of neutron-rich isotopes, e.g., ^{50}Ti, ^{54}Cr, ^{60}Fe, and ^{64}Ni with respect to ^{56}Fe. Such overproduction can be strongly constrained by the galactic chemical evolution. We will further discuss the ejecta properties in Section 4.2.

Combining these three plots, the effective formula of the turbulent flame prescription also plays a role in the ONeMg collapse condition similar to the initial flame size and the properties of the flame kernel. In particular, models tend to collapse (expand) when the flame is slow (fast). This is because the slower flame provides more time for the electron captures, thus allowing the star to contract faster before the flame can burn the matter in the outer regions. On the other hand, the faster flame allows a faster growth of its surface area, which can balance the effects of decreasing $Y_{\rm e}$. At last, we remark that such a flip of results from an expanding model to a collapsing model can be seen only for those near the transition. In Section 4 we further explore the effects of flame physics on other models with different flame geometry.

3.6.1. Extension: Effects of Laminar Flame Propagation

We remark that the treatment of a nuclear flame in the literature does not always assume sub-grid scale turbulent motion (see, e.g., Plewa 2007). The flame is only distorted by the smallest resolvable length scale by the simulation, and it is assumed that the fluid motion below the resolvable scale is laminar (except for the perturbations by Rayleigh–Taylor instabilities). This forms another limit in the flame propagation.

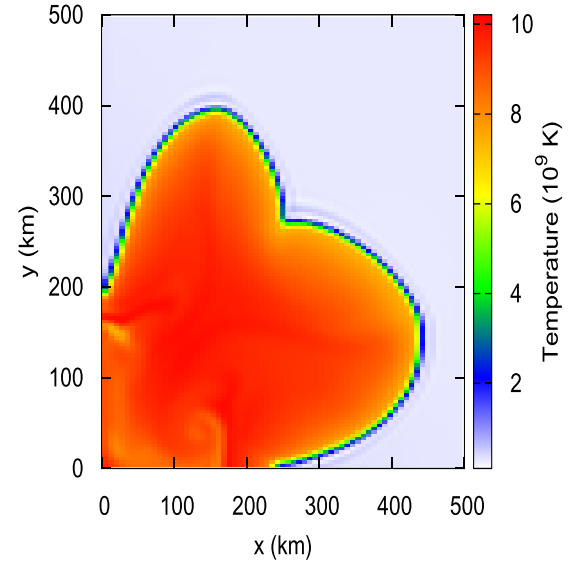

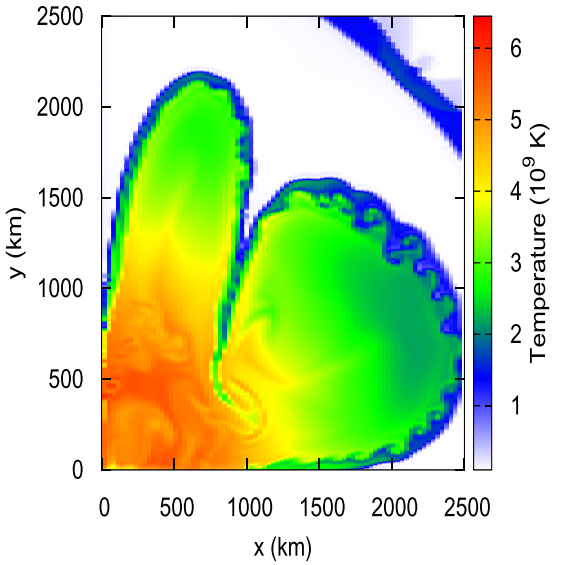

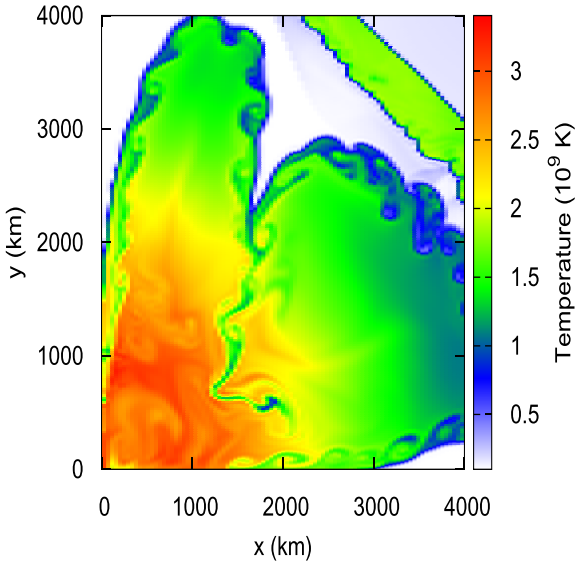

Figure 10. Temperature color plots of model b1b-09950-N at 0.5, 1.0, and 1.25 s of the simulations. The hot regions also represent those being burnt by the ONe deflagration.

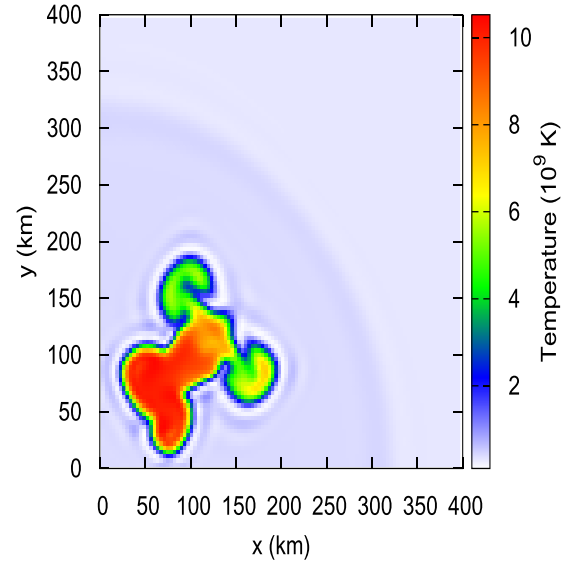

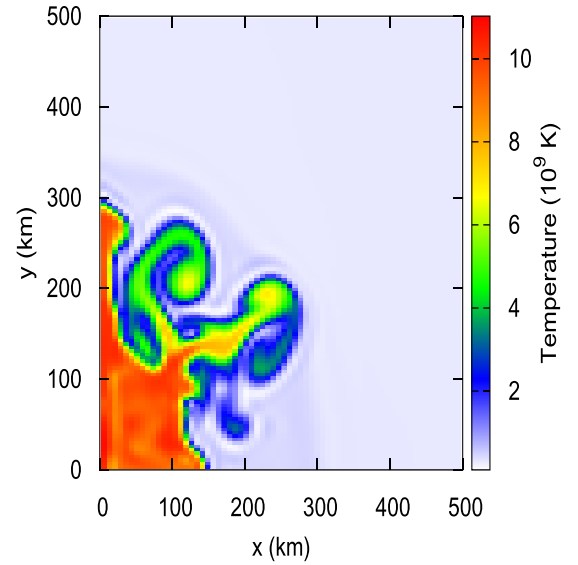

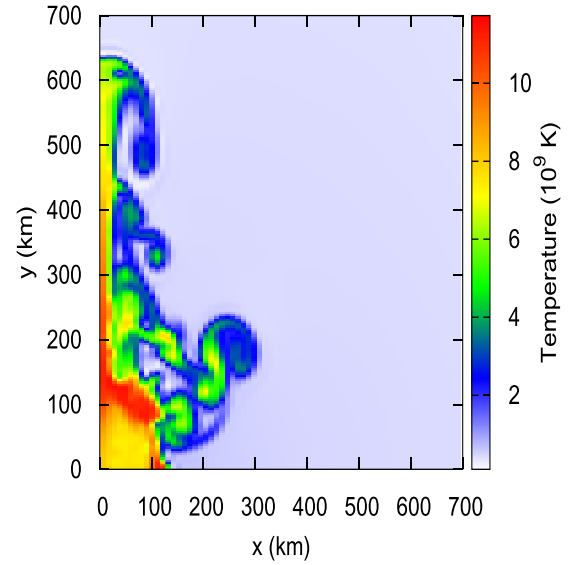

Figure 11. Temperature color plots of model b1b-09950-N-Lam at 0.4, 0.8, and 1.2 s of the simulations. The hot regions also represent the regions being burnt by the ONe deflagration.

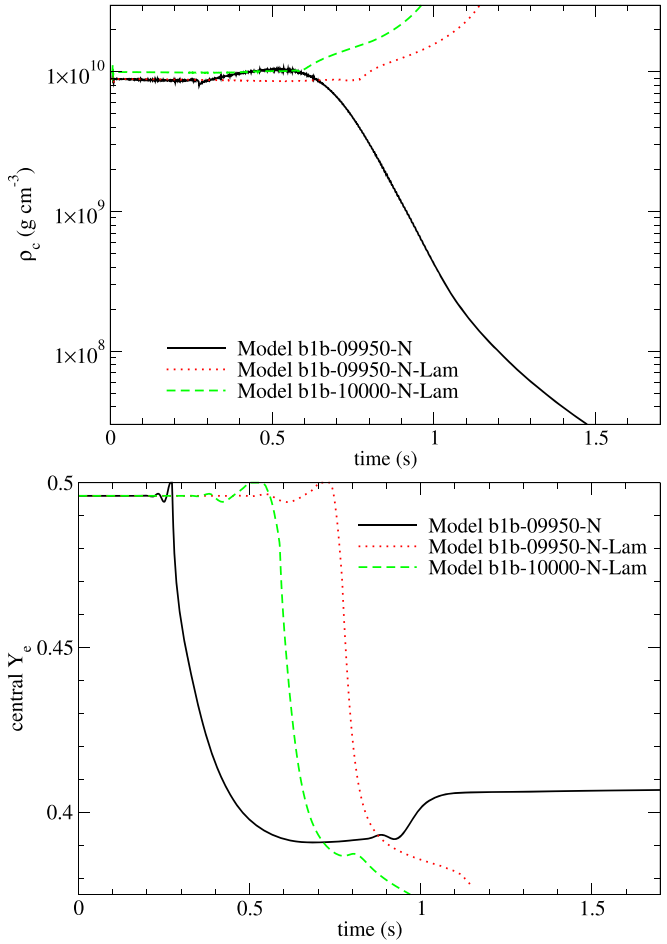

Figure 12. (Top panel) Central densities against time for models b1b-09950-N (ρ_c $10^{9.95}$ g cm^{-3}, turbulent flame), b1b-09950-N-Lam (ρ_c $10^{9.95}$ g cm^{-3}, laminar flame), and b1b-10000-N-Lam (ρ_c 10^{10} g cm^{-3}, laminar flame). (Bottom panel) Same as the upper panel, but for the central Y_e for the same set of models.

To demonstrate this limit, we pick an ONeMg core configuration with an initial flame size which expands in the default setting. Our models, assuming a flame speed much slower than the speed of sound, can have a flame propagation that is more enhanced along the symmetry axis. So, an off-center flame is preferred. We choose models b1b-09950-N-Lam, b1b-09975-N-Lam, and b1b-10000-N-Lam. (An ending "-Lam" corresponds to the flame that only propagates without sub-grid acceleration.) We discuss the effects of the slower flame in general in Section 4.1.

Models b1b-09950-N-Lam, b1b-09975-N-Lam, and b1b-10000-N-Lam collapse into a neutron star. In contrast, we compare model b1b-09950-N-Lam with Model b1b-09950-N. They have the same configurations, but the latter is modeled with a turbulent flame prescription. Model b1b-09950-N expands like a Type 1.5 supernova. On the other hand, when the laminar flame prescription is used, the star directly collapses. This shows that whether or not the flame geometry interacts with the sub-grid scale eddy motion, or only interacts with the buoyancy smearing, changes the collapse–explode bifurcation of the benchmark model $\rho_c = 10^{9.95}$ g cm^{-3}.

To characterize the differences of the flame propagation by the turbulent flame and the laminar flame, we plot in Figure 10 the temperature color plots of model b1b-09950-N from 0 to 1.25 s at selected time points. The hot elements also trace the

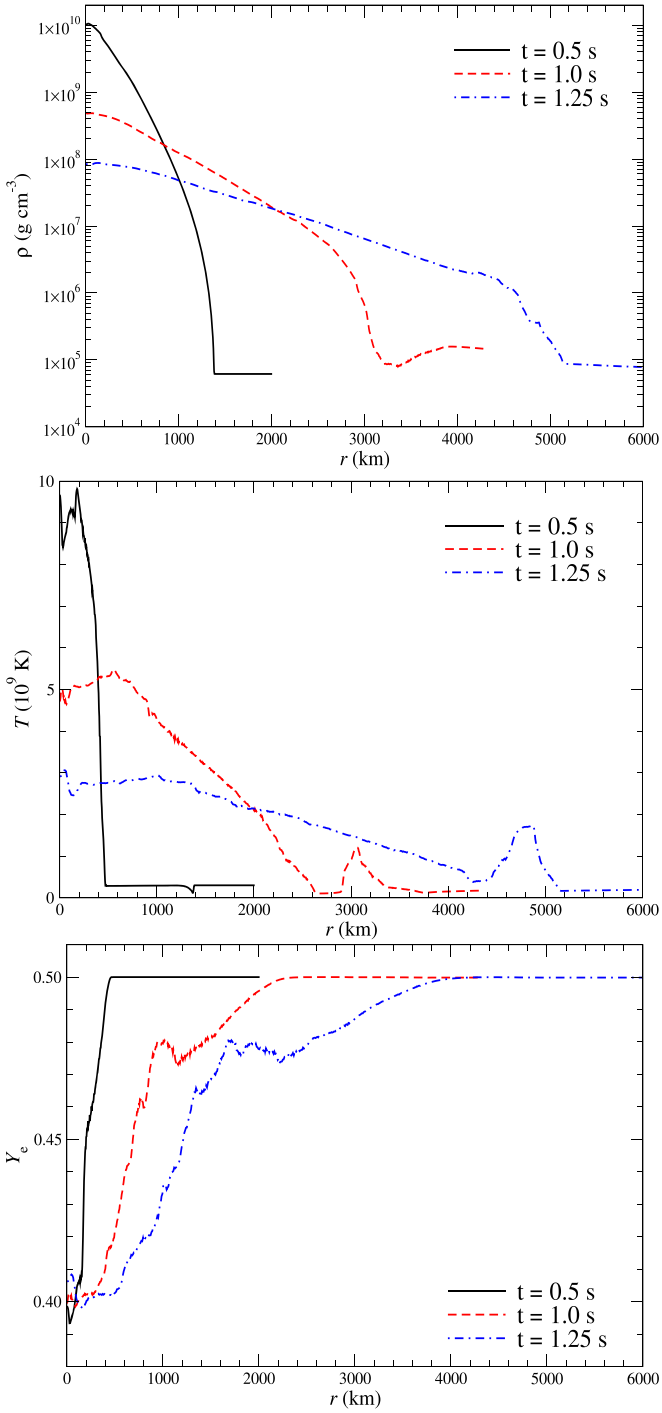

Figure 13. (Top panel) The angular averaged radial density profiles of models b1b-09950-N at $t = 0.5$, 1.0, and 1.25 s. (Middle panel) Same as the top panel but for the temperature profiles. (Bottom panel) Similar to the top panel but for the Y_e profiles.

flame structure. The turbulent flame allows the structure to grow rapidly. Within the first 0.5 s, there is a two-bump structure developed and the size has grown to ∼450 km. At $t = 0.75$ s onward, the large-scale structure freezes and the two-"finger" shape emerges. At $t = 1.0$ s, the flame expands rapidly to 2000 km, where the surface shows more features when the hydrodynamical instabilities become pronounced.

Figure 11 is the same as Figure 10 but for model b1b-09950-N-Lam from 0.2 to 1.2 s at selected time points. A qualitative

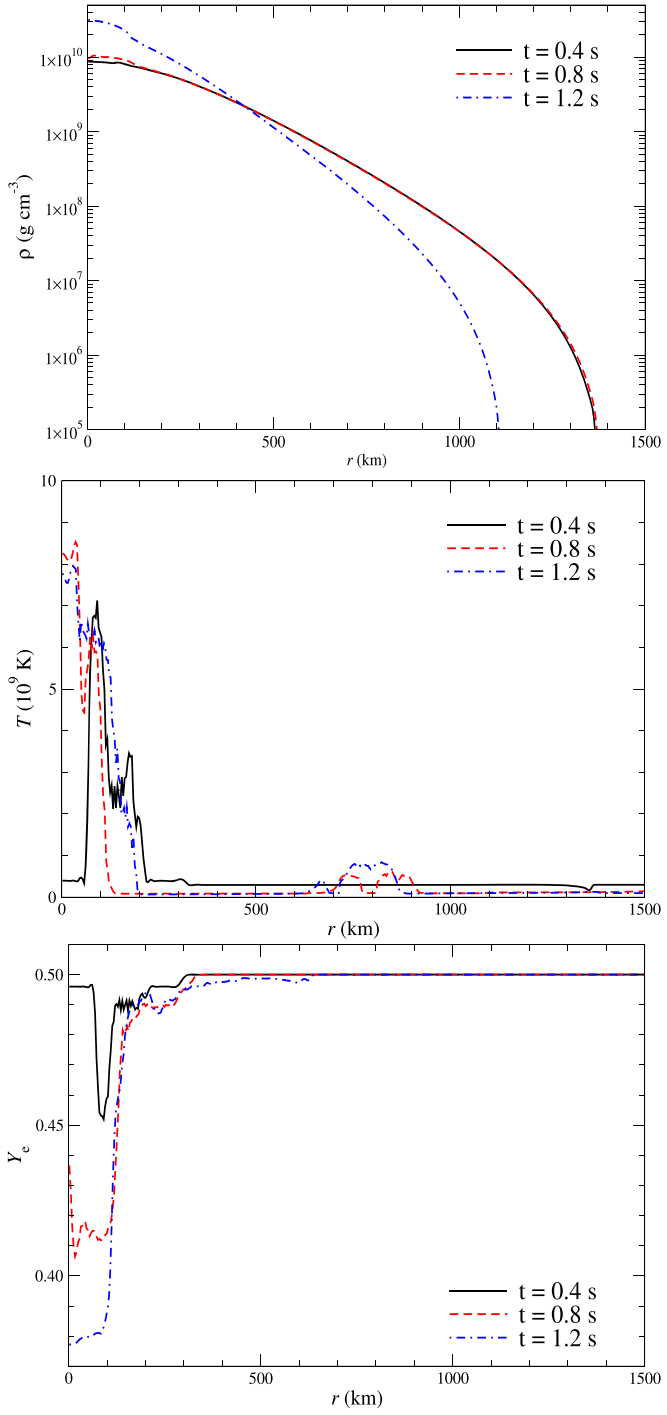

Figure 14. (Top panel) Angular averaged radial density profiles of models b1b-09950-N-Lam at $t = 0.5$, 1.0 and 1.25 s. (Middle panel) Same as the the top panel but for the temperature profiles. (Bottom panel) Similar to the top panel but for the Y_e profiles.

comparison of the flame structure already demonstrates drastic differences between the propagation of the laminar flame and the turbulent flame. At early time before 0.4 s, the fluid motion has largely reshaped the original spherical flame structure. Many small-scale "mushroom shapes" swarm out as a manifestation of the Rayleigh–Taylor instabilities. At $t = 0.6$ s, the flame has finally reached the core, where a hot core of size 150 km can be seen. After that, the core does not grow significantly. However, there is a hot flow along the rotation axis. This is the mentioned enhancement due to Rayleigh–Taylor instabilities along the symmetry boundary. However, this enhancement does not affect the results, as we checked that the burnt mass does not increase significantly. Within another 0.2 s, the core directly collapses.

We further examine their evolution by the quantities in the core. In the upper panel of Figure 12, we plot the central density against time for models b1b-09950-N-Lam, b1b-09975-N-Lam, and b1b-10000-N-Lam. For comparison, we also include the data from model b1b-09950-N. The central densities of models b1b-09950-N and b1b-09950-N-Lam are the same before $t = 0.4$ s, when the flame has not reached the core. Once it reaches the core, namely at $t = 0.4$ s for model b1b-09950-N and at $t = 0.8$ s for model b1b-09950-N-Lam, they deviate from each other. Both models show an increase in central density due to the softening effect by electron capture. However, for model b1b-09950-N, the central density starts to drop beyond $t = 0.6$ s, showing that the turbulent flame has released sufficient energy to support against the inward flows. On the other hand, in model b1b-09950-N-Lam, the increase in the central density leads to the collapse where there is no sign for the core to reach a temporary equilibrium. A similar evolution can be seen in model b1b-10000-N-Lam. After $t = 0.8$ s, where the flame reaches the core, the increase of the central density triggers the collapse.

The lower panel of Figure 12 is similar to the upper panel but for the central Y_e. After the flame has reached the core, which can be noted by the sudden drop of Y_e, the electron captures of the expanding model b1b-09950-N slow down at $t \approx 0.5$ s, and the central Y_e stays at ≈0.39. It later returns to a high value when the core material begins to mix with the higher Y_e material in the outer zone. On the other hand, the Y_e does not reach any equilibrium value once the core is burnt. The local electron-capture rate slows down at $t = 0.9$ s. Model b1b-10000-N-Lam also has a similar pattern. But the fall of Y_e slows down at 0.8 s, showing that the inner part does not collapse directly. The outer matter, which continues to flow inwards, as implied by the growth of the central density, triggers further electron captures, which make the ONeMg core collapse.

Then, we compare the evolution of the two models by plotting the radial profiles. The radial profiles are obtained by calculating an angular average of the related quantities. This allows us to compare directly how the ONeMg core responds under different types of flame, and furthermore how the ONeMg core looks dynamically when it expands or collapses.

In Figure 13, we plot the density, temperature, and Y_e radial profiles for model b1b-09950-N in the top, middle, and bottom panels, respectively. We plot in Figure 14 similar to Figure 13 but for model b1b-09950-N-Lam.

Model b1b-09950-N is an expanding model. The central density of the star quickly drops by two orders of magnitude in ≈1 s. However, the monotonic variation of the density profile in the inner core does not change throughout the simulation. This shows that the deflagration we modeled is quiet enough to suppress acoustic wave generation. On the other hand, there is almost no change in the profile in model b1b-09950-N-Lam, which is a collapsing model. The star contracts homologously until the end of the simulation.

In model b1b-09950-N, the temperature profiles show more features compared to the density profiles. The off-center burning allows the temperature peaks at 100 and 500 km at $t = 0.5$ and 1.0 s. When the star begins its expansion, the off-center temperature peak is smoothed out. Besides that, the

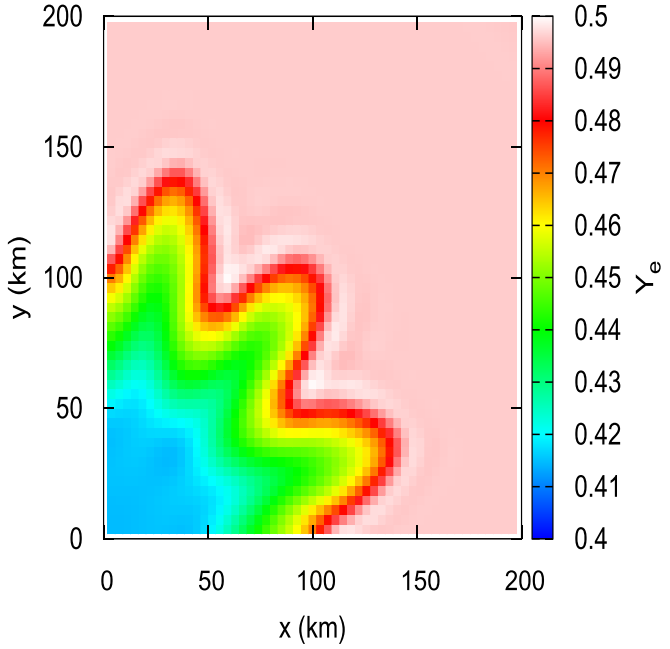

Figure 15. The Y_e color plot of model c3-09950-N-B050 after including the laminar propagation phase.

initial injection of flame creates a small pulse that heats the near-surface matter and creates a small temperature bump at 3000 (5000) km at 1.0 (1.25) s. For model b1b-09950-N-Lam, the flame is still off-center at 0.4 s. A small temperature bump is observed at ~700 km due to the perturbation of initial flame. Until the end of the simulation, the high-temperature region ($T > 3 \times 10^9$ K) is confined within the innermost 200 km.

In model b1b-09950-N, the initial electron captures are confined to the innermost 200 km. Accompanying the expansion, the shape of the Y_e profile is frozen beyond 1.0 s, where the expansion elongates the profile. For model b1b-09950-N-Lam, the slow "laminar" allows more transport of Y_e before rapid electron captures take place. The electron captures at $t = 0.8$ and 1.2 s are localized in the innermost 100 km and carry on until the end of simulation.

3.7. Effects of Pre-runaway Time-lapse

In our simulations, the initial flame we impose is limited by the size of the resolution grid (~4 km). However, it is unclear whether the flame is triggered at this size, or at a size smaller than the grid resolution. In fact, in Timmes & Woosley (1992), the size of flame in mass can be as small as 10^3–10^{17} g, depending on the local temperature, such that the runaway can occur spontaneously. This means that the initial runaway can have a size much smaller than the typical resolution (~km) when the first nuclear runaway starts. Therefore, there can be a time-lapse between the "first" nuclear runaway and the flame structure we used. The time-lapse allows the Y_e inside the runaway to be different from its initial value. To account for this lapse, we prepared models with a much smaller *c*3 flame (for a few grids to make the flame shape well resolved by the level-set method). The flame is then allowed to expand self-similarly until it becomes the size and the shape of the *bc*3 flame. Meanwhile, all nuclear reactions, such as photodisintegration of ^{56}Ni into ^{4}He, and electron capture, can proceed. After the flame reaches the size of the *bc*3 flame, the fluid advection of the flame is resumed. This attempts to mimic the

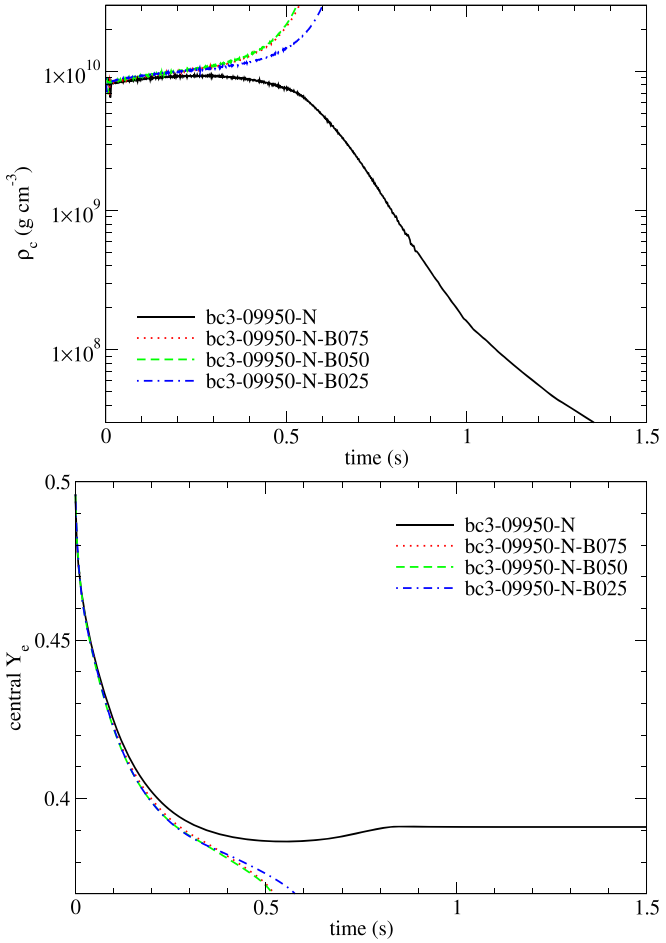

Figure 16. (Upper panel) Evolution of central density against time for model bc3-09950-N (default flame size), bc3-09950-N-B075 (75% flame size), bc3-09950-N-B050 (50% flame size), and bc3-09950-N-B025 (25% flame size). All models share the same initial flame geometry *bc*3 and initial central density $10^{9.95}$ g cm^{-3}, and they assume Newtonian gravity. (Lower panel) Same as the upper panel but for the central Y_e.

laminar phase where the flame grows self-similarly without being perturbed by the fluid motion.

In this series of models, we change the initial size of the flame from 25%–75% of the original flame used in the *c*3 Model series. We choose the largest flame model because we want to contrast the effects of the time-lapse in the initial laminar phase. Again, we use the *bc*3 as the template because it has a sufficiently large size such that we can construct a similar flame structure of smaller size for comparison. Also, the effects of this treatment can be more clearly observed near the bifurcation density, which is near $10^{9.95}$ g cm^{-3} for the *bc*3 flame. When a smaller flame is used, models with lower initial ρ_c are necessary to see the changes. We stick to $10^{9.95}$ g cm^{-3} because it is the typical runaway density predicted from the stellar evolutionary models using the Ledoux criterion.

In Figure 15, we plot the Y_e of model c3-09950-N-B050 at the moment we allow the deflagration to follow the fluid motion when the flame reaches the required size. It takes ~125 ms for the flame to reach from half of its size (about 60 km) to the current size. The *c*3-flame is chosen as described above. Near the flame surface, since the weak interaction is slow, most matter keeps its initial Y_e. Around $r = 80$ km, the Y_e quickly drops from 0.50 to ~0.44. Within the innermost 40 km, the Y_e can drop as low as 0.40–0.42.

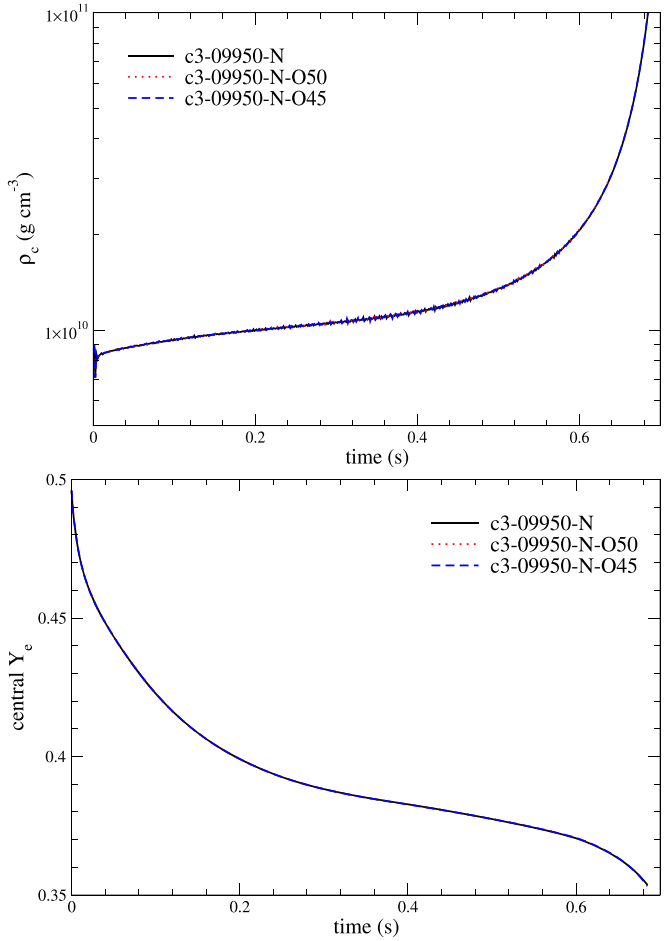

Figure 17. (Upper panel) Evolution of the central density against time for models c3-09950-N (default ^{16}O ratio), c3-09950-N-O50 ($X(^{16}\mathrm{O}) = 0.50$), and c3-09950-N-O45 ($X(^{16}\mathrm{O}) = 0.45$). All models share the same initial flame geometry $c3$ and initial central density $10^{9.95}$ g cm^{-3}, and they assume Newtonian gravity. (Lower panel) Same as the upper panel but for the central Y_e.

In the upper panel of Figure 16, we plot the evolution of central density against time for models bc3-09950-N, bc3-09950-N-B075, bc3-09950-N-B050, and bc3-09950-N-B025. Model bc3-09950-N explodes while the other three models collapse. In the first 0.2 s, all four models share a similar ρ_c evolution. However, beyond that time, the values of ρ_c in the latter three models are slightly higher, which lead to their later collapse at 0.5–0.6 s.

In the lower panel of Figure 16, we plot the central Y_e evolution for the same set of models. The three collapsing models show a qualitatively similar pattern as those in previous sections. However, they all share a lower Y_e compared to the exploding model bc3-09950-N. This is related to the difference in the relaxation of the initial flame by isobaric expansion.

The models considering the effects of pre-runaway time-lapse show that the ONe core evolved from the stellar evolutionary model is likely to collapse into a neutron star and create an ECSN, but the exact details still strongly depend on the pre-runaway scenario, where the electron captures in the sub-grid scale are important for the initial Y_e profile and also its subsequent dynamics. We also remark that despite the flame structure of flame c3-09950-N and bc3-09950-N-B025 being the same, they are not identical because bc3-09950-N-B025 has more time for electron captures during the enforced laminar flame phase. Also, the frozen flame shape during the laminar phase in Model bc3-09950-N-B025

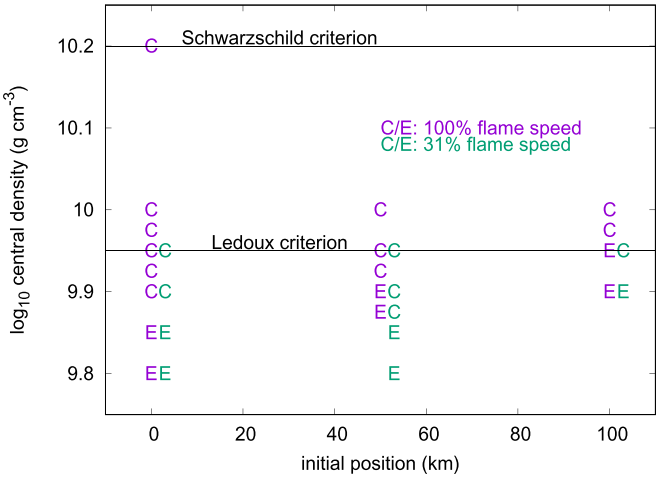

Figure 18. Phase diagram of the collapse-expand bifurcation for the models studied in this work. 'C' and 'E' correspond to the models which collapse and expand, respectively. The X- and Y-positions of the letter correspond to the flame position (0, 50 and 100 km) and initial central density ($10^{9.8}$–$10^{10.2}$). Models for two contrasting flame speeds at 100% and 31% are shown as the left (purple font) and the right (green font letter). The upper (lower) line corresponds to the runaway density predicted by the Schwarzschild (Ledoux) convection criteria.

causes a different turbulent energy distribution when the flame can propagate freely compared with model c3-09950-N.

3.8. Effects of Initial ^{24}Mg

In Section 2, we discussed that we do not include ^{24}Mg in the raw fuel because there is numerical difficulty in how to distinguish ^{24}Mg from the fuel and from the ash. The replaced composition may overestimate the energy production. In previous sections, we have shown that the actual results are sensitive to multiple parameters in the configuration. Here, we further examine how the choice of the initial composition affects the collapse-explode bifurcation. In particular, we study how the initial abundance of ^{24}Mg affects the final evolution of ECSN.

To characterize the effects of the initial composition on the final fate of ECSN, we construct ONe cores using the uncertainties of the mass fraction of ^{16}O as a model parameter at the same initial central density ($10^{9.95}$ g cm^{-3}). After that, we ignite ONe core with an identical initial flame $c3$. In all previous models, the initial ^{24}Mg, which has captured electrons to form ^{24}Ne, is regarded as part of the ^{16}O. Here, we variate the initial model and treat the ^{24}Ne as part of the ^{20}Ne or both ^{16}O and ^{20}Ne by half. Besides the initial model, the initial composition also affects the laminar flame speed (see, for example, the ^{12}C- and ^{16}O-dependence of the laminar flame speed in Timmes & Woosley 1992.) The energy production when the fuel is burnt completely to NSE is also adjusted according to the initial composition. For a higher ^{16}O initial mass fraction, the laminar flame speed is higher, and the energy production is also higher.

In Figure 17, we plot in the upper and lower panels the central density and Y_e against time, respectively, for the three models described above. In general, the three curves overlap each other. No observable changes can be seen from the onset of nuclear runaway until the end of the simulations. This shows that the change in the initial composition does not affect the final fate of ECSN, in the uncertainties considered

Table 3
Comparison of Input Physics and Numerical Setting between Our Work and Those in Jones et al. (2016)

Physics Component	Our Work	Jones et al. (2016)
Numerical code	Leung et al. (2015a)	LEAFS
Dimensionality	2D	3D
Coordinates	Cylindrical	Spherical
Spatial discretization scheme	WENO (fifth order)	PPM (third order)
EOS	Helmholtz	Individual prescription
Sub-grid turbulence	Niemeyer et al. (1995)	Schmidt et al. (2006)
Energy scheme (in Hydro)	three-step burning with NSE	one-step burning with NSE
Hydro isotope network	7	5
Flame capturing scheme	Level-set methods	Level-set methods
Post-processing isotope network	495	N/A
Electron-capture rate	Extension of Seitenzahl et al. (2010)	Extension of Seitenzahl et al. (2010)
Nuclear reaction rate	Langanke & Martinez-Pinedo (2001)	N/A

here. Similar results can be found for the central Y_e. The drops of Y_e for the three cases do not show variations from each other. As both figures show, it suffices to say that treating the neglected ^{24}Mg as part of the initial ^{16}O or as part of the initial ^{20}Ne does not bring any qualitative change to our results.

4. Discussion

4.1. Global Properties of ONeMg Core

In previous sections, we have compared the final evolution of ONeMg cores with different input physics. We find that the initial central density, flame position, and flame speed are important for determining the final fate of the star. In this section, we summarize the models by building a phase diagram of them.

In Figure 18, we plot the phase diagram of the collapse-expand bifurcation of our models with the initial flame position and the initial central density as the x- and y-coordinates. Two contrasting flame speeds, the default one and a reduced one, at an asymptotic value of 31% of the default value, are shown. We mark the figure with two horizontal lines that characterize the runaway densities using the Ledoux ($10^{9.95}$ g cm^{-3}) and Schwarzschild criteria ($10^{10.2}$ g cm^{-3}). These are the expected runaway densities taken from the literature (see, e.g., Miyaji & Nomoto 1987; Schwab et al. 2015). We focus on models near the bifurcation point. Once the transition is located, models with initial central densities above that collapse and those below expand. All models with an initial central density $>10^{9.95}$ g cm^{-3} collapse for the centered flame and off-center flame at 50 km from the origin. A higher transition density at $10^{9.975}$ g cm^{-3} is observed when the flame starts at 100 km from center. This suggests that ONeMg models using the Schwarzschild criterion, i.e., an ignition density of $10^{10.2}$ g cm^{-3}, collapse for both centered and off-center flames. ONeMg models using the Ledoux criterion, i.e., an ignition density of $10^{9.95}$ g cm^{-3} collapse, when the first flame starts within the innermost 50 km. However, we remind the reader that the convection after the onset of core O-burning, even in the Ledoux criterion, could delay the nuclear runaway substantially. The value $10^{9.95}$ g cm^{-3} should be treated as a lower limit.

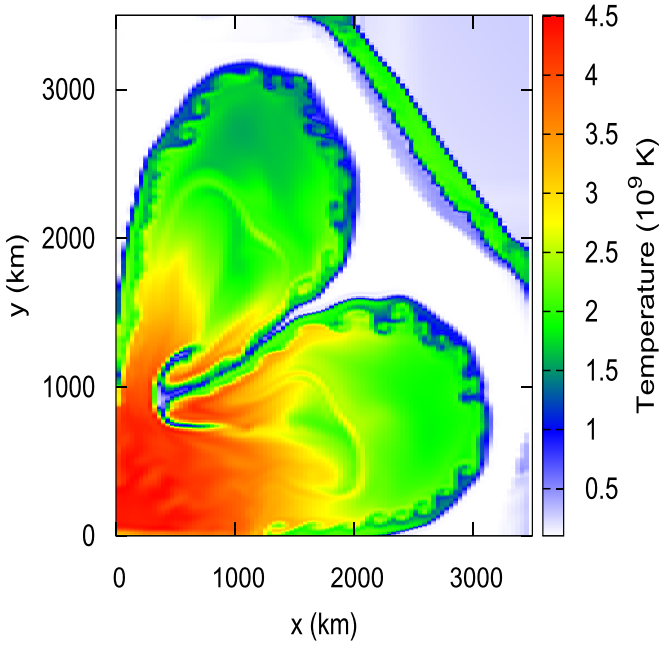

Figure 19. Temperature profile of Model bc3-09950-N at 1 s of the simulation. Notice that the flame is highly irregular with the signature from Rayleigh–Taylor instabilities and Kelvin–Helmholtz instabilities.

By examining the distribution of "C"s in the diagram, we find that the majority of models still collapse into NSs. In the parameter range surveyed in this work, the initial flame position affects primarily the variations of the transition density, compared to the variations of the turbulent flame speed formula. A change of the transition density in the $\log_{10}$ scale by 0.075 can be observed for different initial flame positions but only 0.025 for different turbulent flame speed formulas.

This diagram demonstrates the diversity of the possible outcomes of the ONeMg core, even when they are prepared in a very similar way in terms of mass, flame geometry and flame position. It demonstrates the necessity of future stellar evolutionary work in a better modeling of the convective process before the runaway. This includes (1) the pre-runaway configuration by the detailed nuclear runaway position, (2) its initial nuclear runaway size in mass, and (3) the ONeMg core Y_e profile and its composition.[5]

We also remark about the divergence of results among models with a $c3$, $mc3$, or $bc3$ flame. They demonstrate the importance of how the collapse depends on the global motion of the ONeMg core. We showed that models with a $c3$ flame have a longer time for the onset of collapse than those with an $mc3$ flame, while those with a $bc3$ flame expand. The small $c3$ flame requires a longer time for the development of flame until global contraction is triggered. On the other hand, the larger

[5] In this work, we have not explored in detail the role of the initial Y_e. The details of the Y_e depend on the treatment of convective mixing after the hydrostatic O-burning has started. The mixing can compensate the drop of the Y_e by the electron captures of ^{16}O and ^{20}Ne. Such details can be provided by the stellar evolutionary models, but numerical difficulties for resolving the hydrostatic O-burning front under convective mixing make such prediction difficult. In fact, in Section 3.7, by using the pre-conditioned flame with initial Y_e differences, the initial Y_e can affect the transition density of ECSN.

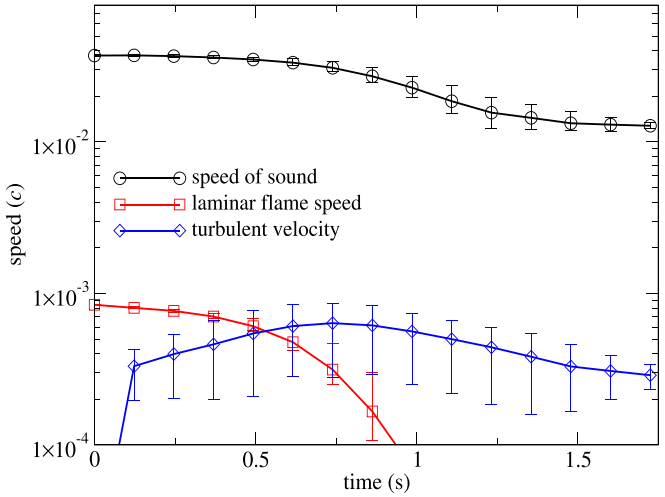

Figure 20. Speed of sound, laminar flame speed, and turbulent flame speed for model c3-09850-N shown in Figure 3. The lines stand for the mass-averaged values from the grids where the flame surface can be found. The error bars show the maximum and minimum flame speeds found in simulations at the corresponding time points.

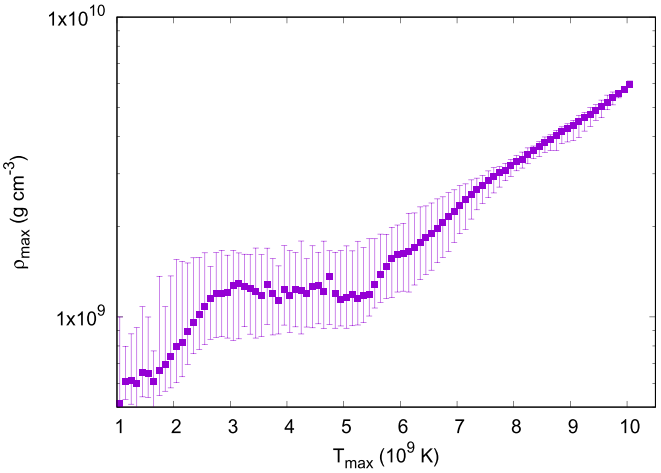

Figure 21. Maximum density $\rho_{\max}$ against maximum temperature $T_{\max}$ for the tracer particles in model c3-09800-N. The error bars stand for the range of $\rho_{\max}$ of the tracers in the same bin of $T_{\max}$.

*mc*3 flame allows more electron captures to take place in the ash. This accelerates the global contraction.

4.2. Comparison with Literature

Since there is no explicit work in the literature except Jones et al. (2016) on the multidimensional simulations of ECSN, we compare our hydrodynamical results with theirs. In Table 3, we list the input physics and configurations used in their work and this work. Overlap in microphysics is attempted to make the comparison of results easier. However, some fundamental infrastructure, including the hydrodynamical solvers, equation of states, and nuclear reaction schemes are different.

First, we examine the threshold density for the expand-collapse bifurcation. Our models show that a central ignited flame has a transition density at $10^{9.9}$ g cm^{-3}, which increases to $10^{9.975}$ g cm^{-3} when the flame distance from the center increases from 0 km to 100 km. In the six models presented in Jones et al. (2016) with a ρ_c at $10^{9.90}$, $10^{9.95}$ and $10^{10.2}$ g cm^{-3}, the first two models expand and the last one collapses. Given that they use a different flame structure ($\sim$100 flame bubbles with a total mass $\sim 10^{-3}\,M_\odot$ burnt) at the beginning, our results agree qualitatively with theirs by considering their representative flame distance, initial burnt mass, and central densities. Also, their model with $\rho_{\rm c,ini} = 10^{10.2}$ g cm^{-3} has a collapse time around 0.3 s, which also agrees with ours (0.26 s; see for example Figure 7 for the evolution of central density).

Then we compare the flame morphology. In their work, they show the flame structure in Figure 6 and the cross-section cut in Figure 7. We compare these with our results in Figure 19. The outburst of flame in the spherical shape with Rayleigh–Taylor instabilities and their induced small-scale sub-structures can be seen in both works. Because our model has a coarser resolution compared to their work, the flame structure in our model shows fewer sub-structures than theirs.

At last, we compare the time evolution of a turbulent flame. In Figure 20, we plot the speed of sound, laminar flame speed, and turbulent flame speed of the model c3-09850-N. The data is taken from a grid point that is actively burning by deflagration. In the beginning, the laminar flame is dominant because we assumed an ONeMg core in hydrostatic equilibrium. We note that in their work, the turbulent flame speed is slower than that in ours. It is because, in the formalism from Pocheau (1994), the minimal turbulent flame speed is always the laminar flame speed. We estimate that the turbulence velocity is comparable with the flame speed for $t < 0.2$ s.

The turbulent flame speed quickly exceeds the laminar flame and reaches an equilibrium value of $\sim O(10^{-2})$ of the speed of sound. This figure can be compared with Figure 4 in the Jones et al. (2016) G13 model but with three differences. First, they used three-dimensional Cartesian coordinates, and we use two-dimensional cylindrical coordinates. Their three-dimensional simulations may allow for a more complex flame structure in the simulation. The higher-dimensional simulation allows for a more flexible choice of the initial flame with less concern of enhancement by a particular boundary condition. Second, the sub-grid-scale (SGS) model is based on the formalism in Schmidt et al. (2006), while ours is based on the scheme in Niemeyer et al. (1995). Both models belong to the class of one-equation model but with different closures. Third, their models start from a number of off-center bubbles, while, due to symmetry, we choose a centered flame as the initial flame structure. Our "three-finger" structure helps to enhance the turbulence by the initial asymmetrical flow. This allows our model to reach the turbulent regime faster than theirs, resulting in more vigorous nuclear burning. On the other hand, the bubble structure, where bubbles are geometrically isolated at the beginning, makes the generation of turbulence slower because of the initially isotropic expansion of the bubble. Even with very different sub-grid turbulence models, the results are qualitatively similar, such as the asymptotic value and the range of turbulent flame speed found in the simulation. One major difference is the time when turbulence becomes saturated owing to our choice of initial flame. We choose the *c*3 flame, as was done in Reinecke et al. (1999). At last, in our simulations, the reflective inner boundaries of both planes can create boundary flows, which can also enhance the SGS turbulence production. Future extension of our work using three-dimensional simulations and with similar flame structure and resolution, will provide more rigorous constraints on the collapse-expand transition boundary.

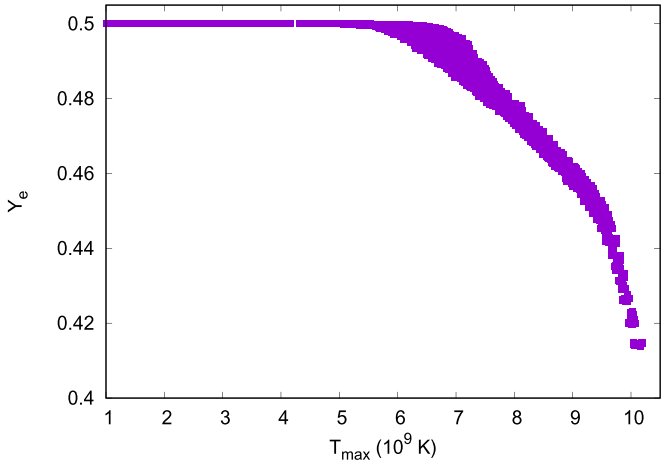

Figure 22. Final Y_e against maximum temperature T_{max} for the tracer particles for the model c3-09800-N.

4.3. Electron-capture-triggered Thermonuclear Explosion

Here, we discuss the properties of the exploding models, and then we analyze the possible nucleosynthesis signature of the exploding models. We analyze the thermodynamics history of one of the expanding models c3-09800-N by studying the tracer particles.

First, we plot in Figure 21 ρ_{max} against T_{max} derived from the tracer particles in the simulations. The maximum density and temperature are defined by the maximum values experienced by the particles throughout their history from the onset of the flame until the expansion. The distribution is separated into three parts. The first part is a monotonically increasing trend above high $T_{max} \sim 6 \times 10^9$ K. The second part is an approximately constant ρ_{max} at intermediate $T_{max} = (3\text{–}6) \times 10^9$ K, and the third part is another monotonic increasing trend at low $T_{max} < 3 \times 10^9$ K. The tight relation for high T_{max} is consistent with typical Type Ia supernovae exploded by pure turbulent deflagration. The sub sonic deflagration wave does not generate any strong sound wave, which can increase the spread of T_{max} for a given ρ_{max}. Also, most inner parts of the core are burnt at the same time by the centered flame. On the other hand, in the intermediate T_{max} regime, the flame becomes aspherical in that the fluid elements with the same initial density can experience different levels of time-delay when the flame arrives. The low T_{max} regime corresponds to where the flame is quenching at $\rho \sim 10^9$ g cm^{-3}. The value is higher than that for CO matter because the typical energy release for the burning of the ONe matter is lower.

Then, we plot in Figure 22 the Y_e distribution of the tracer particles as a function of ρ_{max}. The distribution consists of two parts. For the tracer particles that experienced electron capture ($T > 5 \times 10^9$ K), the final Y_e drops when T_{max} increases. The lowest $Y_e \sim 0.41$ are obtained by the particles having the highest temperature $\sim 10^{10}$ K in their thermodynamic history. A small spread can be seen for particles close to the NSE transition temperature. Again, this is related to the aspherical flame propagation.

Since the electron-capture rate is much slower than the dynamical timescale, the final Y_e determines the isotopes in the ejecta. At such low Y_e, neutron-rich isotopes such as ^{48}Ca ($Y_e = 0.41$), ^{54}Cr ($Y_e = 0.42$), ^{60}Fe ($Y_e = 0.43$), and ^{64}Zn ($Y_e = 0.47$) are the representative stable isotopes. The relative Y_e for Zn is high, but the high entropy environment enhances the formation of this particular isotope compared to the SN Ia counterpart. See, for example, Wanajo et al. (2018) and Jones et al. (2019). As discussed in Nomoto & Kondo (1991) and Woosley (1997), these isotopes are not consistently produced in ordinary SNe Ia. These isotopes, if ejected, can provide tight constraints on the relative rate of ECSNe to other types of supernovae.

We do not attempt to do the nucleosynthesis as in our previous work because a longer period of time after the explosion ($\sim$10 s) is necessary to distinguish the tracers that are ejected and tracers that fall back to form the remnant. Without this information, the final yield might overestimate the final masses of iron-peak elements, which are more likely to fall back when the fluid elements move outwards and expansion, which transport their momenta from the core to the envelope.

Furthermore, after the expansion takes place, the ONeMg core partially ejects its matter. The ejecta may contain elements from both the ONe-rich fuel and the Fe-rich ash produced in the ONeMg core. The remaining matter becomes a lower-mass remnant. In Jones et al. (2016), a typical mass of $\sim 1.2\,M_\odot$ of the remnant is recorded. The lower-mass remnant may coincide with the low-mass SiFe-rich WDs observed (Raddi et al. 2018). In Jones et al. (2019), they further computed the nucleosynthesis yield using a large nuclear reaction network. In our future work, we will compare our nucleosynthesis yield with theirs and perform a detailed analysis for different progenitor masses and flame structures.

4.4. Conclusion and Future Work

In this work, we model the final evolution of the oxygen–neon–magnesium (ONeMg) cores using two-dimensional hydrodynamical simulations. Based on the temperature and Y_e profiles as functions of mass coordinates obtained from stellar evolutionary models, we construct the ONeMg core in hydrostatic equilibrium with a range of central densities from $10^{9.8}$ to $10^{10.2}$ g cm^{-3}. We follow the ONe deflagration phase to examine in which conditions the ONeMg core can collapse into a neutron star.

We surveyed ONeMg core models of various configurations. They include central densities between $10^{9.80}$ and $10^{10.20}$ g cm^{-3} and different flame structures with masses between 10^{-4}–$10^{-2}\,M_\odot$ in a centered or off-centered ignition kernel. We also explore the effects of input physics, which include the relativistic corrections in gravity, turbulent flame speed formula, and the treatment of the laminar deflagration phase. We find that except the general relativistic effects, the latter two can strongly affect the collapse condition. The exact transition density depends on the input physics, but we find that the ONeMg core can collapse with an initial central density with a range from $10^{9.90}$ to $10^{9.975}$ g cm^{-3}. This is consistent with the current picture of stellar evolution that the ECSNe evolved from stars of masses 8–10 $M_\odot$ could be the origin of the lower-mass branch of the neutron star population.

We study how the input physics affects the bifurcation condition of the ONeMg core. Besides the sensitivity of the models to the initial mass as reported in the literature, for the models with the same initial central density, a centered flame favors the collapse scenario. A slower flame (laminar flame or less effective turbulence models) also favors the collapse scenario. A pre-conditioned flame is also favorable to the collapse branch. However, relativistic corrections in gravity and the exact abundance of ^{24}Mg do not play the main role in the evolution of the deflagration phase.

We presented a phase diagram for the collapse-expansion bifurcation for models with a range of central densities, flame

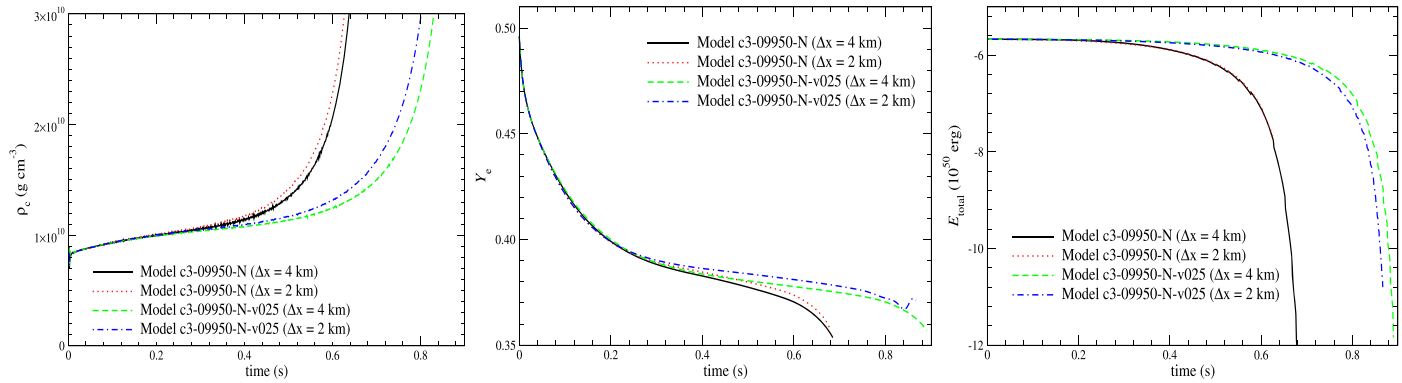

Figure 23. (Left panel) The central density for models c3-09950-N, c3-09950-N-fine, c3-09950-N-v025, and c3-09950-N-v025-fine. (Middle panel) Similar to the left panel but for the central Y_e. (Right panel) Similar to the left panel but for the total energy.

positions, and turbulent flame speeds. We studied the thermodynamics history of the ECSN and discussed its nucleosynthic implications. We also carried out a detailed comparison of our models with the representative models in the literature. Our results suggest that it is necessary to carefully put in treatments like the pre-runaway convection in the stellar evolution of ONeMg core, the turbulent flame modeling, and the mapping from stellar evolutionary models to hydrodynamical simulations to determine the final fate of super-AGB stars after electron-capture-induced nuclear runaway has started. In the stellar evolution theory, these treatments include:

(1) the exact runaway position of the O–Ne deflagration, whether it is centered or off-center, and its size;

(2) the convective mixing and its velocity structure in the ONeMg core before nuclear runaway;

(3) the detailed Y_e profile;[6]

(4) the chemical composition, especially the residue ^{12}C and ^{16}O/^{20}Ne mass fraction ratio in the ONeMg core.

The following improvements may enhance the predictability of our models:

(1) the empirical formula between local velocity fluctuations and the corresponding flame propagation speed,

(2) the detailed velocity spectra of the sub-grid scale eddy motion and its impact on flame geometry.

This work was supported by World Premier International Research Center Initiative (WPI), MEXT, Japan, and JSPS KAKENHI grant Nos. JP26400222, JP16H02168, and JP17K05382. S.C.L. also acknowledges funding by the grant HST-AR-15021.001-A. We thank the developers of the stellar evolution code MESA for making the code open-source.

We thank the anonymous referee for the very detailed and constructive comments that improved this article. We also thank our colleagues who kindly spent their time to help us improve the writing of this article.

We thank F. X. Timmes for his open-source microphysics algorithm including the Helmholtz equation of state subroutine, the torch nuclear reaction network designed for an arbitrary choices of isotopes, the seven-isotope nuclear reaction network. We also thank Ming-Chung Chu for the initial inspiration of building the hydrodynamical code. We also thank H. Shen for her open-source equation of state for the nuclear matter. We thank Christian Ott and Evan O'Connor for the equation of state (EOS) driver for reading the HShen EOS and their open source data for the parameterized electron capture value before bounce. We thank Shuai Zha for his discussion of the preliminary results of his pre-runaway models.

Appendix A
Resolution Study of the Code

In this work, we have performed a number of simulations using the same resolution at ∼4 km. It has been a matter of issue how the results depend on the resolution, especially in simulations of this kind, which rely on input physics involving grid size as the input parameter (e.g., sub-grid scale turbulence). To understand the validity of our results, we attempt to rerun the benchmark model (model c3-09950-N) and its counterpart with a slower flame speed (model c3-09950-N-v025) in a finer resolution at ∼2 km. We denote this model as model c3-09950-N-fine and model c3-09950-N-v025-fine, respectively. We also compare the models using slower flame because the slower flame takes longer time for the collapse to occur. This provides more time for the propagation of the flame, which may amplify the resolution effects.

In the left panel of Figure 23, we plot the central density evolution of the two models. The evolution of the first 0.5 s of the models c3-09950-N and c3-09950-N-fine is almost identical. Similar patterns can be seen for the pair of models c3-09950-N-v025 and c3-09950-N-v025-fine. However, the models deviate from each other where the central density of the finer model grows faster. Despite that, both models stop at a time of ∼0.62 and 0.82 s with a difference ∼1%, when the central density reaches the threshold defined in the code.

In the middle panel of Figure 23, we plot the central Y_e evolution for the four models. The central Y_e of the two pairs are very similar to each other at early time. There is a small bump for model c3-09950-N-v025-fine, which may be originated from resolved mixing with outer meshes, which have a higher Y_e in general.

In the right panel of Figure 23, we plot the energy evolution for the two comparison models. The model pair based on model c3-09950-N-v025 shows a very similar evolution, except near the end. Both models show a sharp drop of total energy near the end of simulation due to the neutrino loss and energy loss by electron captures. The model with a finer resolution shows an earlier drop in the energy consistent with the central density evolution. On the

[6] In this work, we do not explicitly use distinctive initial Y_e profiles. However, in Section 3.7, we demonstrated how the initial laminar phase can change the bifurcation criteria. The laminar phase contributes to a distinctive Y_e profile when the turbulent flame is evolved (see Figure 15). This provides the first indication that even when an identical flame structure is used, the differences in the Y_e profile can alter the final fate of that stellar model.

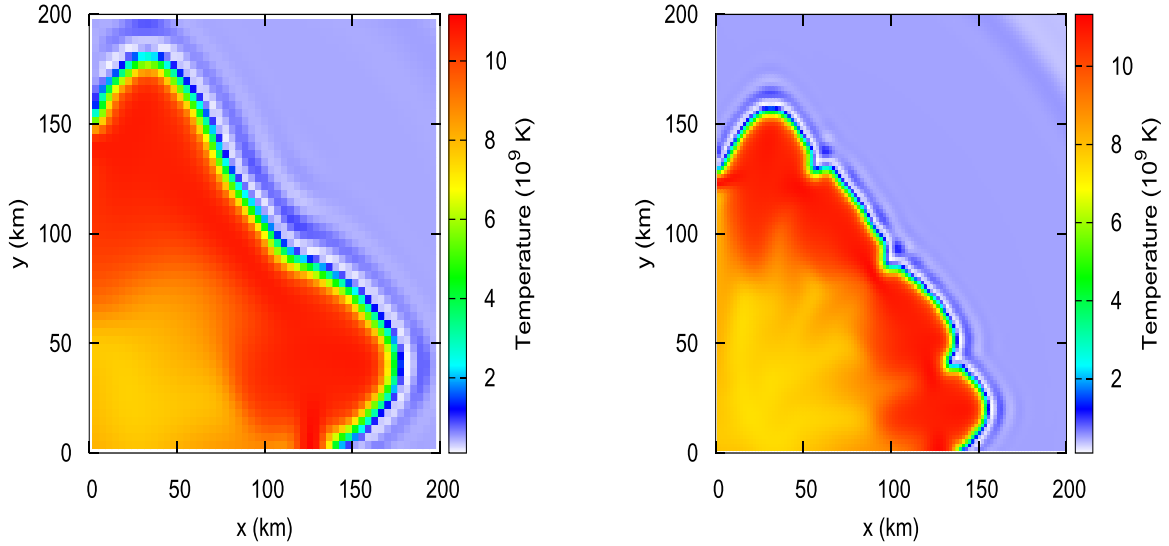

Figure 24. (Left panel) The temperature color plot of the Model c3-09950-N-v025 at 0.75 s after the deflagration has started. (Right panel) Similar to the left panel but for the model at c3-09950-N-v025-fine.

contrary, the energy curves of the model pair based on model c3-09950-N almost overlap each other.

We can see from the results that a finer resolution, in general, allows for faster energy production. This suppresses the effects from electron capture and, hence, the rate of contraction. To further understand the role of resolution size in our simulations, we plot in left and right panels of Figure 24 the flame structure of the two models at 0.75 s after the simulations have started. The flame structure of the two models are of similar shape. The initial "three-finger" structure is smoothed out by the electron captures. The model with a higher resolution shows more features on the front than the lower resolution. However, the flame size is slightly larger for the lower-resolution model by 20%. The core cooled by electron capture is on the contrary smaller in the same model. Such difference can attribute to the different contraction rate, whereas the lower-resolution model, due to a more extended flame, needs more time for accumulating sufficient matter for the final collapse. Despite the difference, the flame structure shows that the current resolution can produce very consistent results, despite that a more rigorous proof with a resolution of even smaller Δx will be needed to verify the convergence.

Appendix B
Possible Observational Signals for the Collapsing Model

In this section, we estimate the following evolution for models that collapse into a neutron star. We remap our models from the two-dimensional cylindrical grid to the one-dimensional spherical grid by doing an angular average. Then we carry out one-dimensional hydrodynamical simulations from the collapse until bounce occurs.

In Table 4, we list the input physics for doing the 1D modeling in the collapse phase. In the 1D simulation, we use the same WENO fifth-order shock-capturing scheme and the three-step third-order NSSP-RK scheme for spatial and temporal discretization. For the EOS, we use the HShen EOS (Shen et al. 1998), which is based on the relativistic mean-field model to describe the homogeneous phase of matter. The table includes extension with the Thomas–Fermi approximation to describe the inhomogeneous matter composition. The parameter for the incompressibility of nuclear matter is 281 MeV and the symmetry energy has a value of 36.9 MeV. Before bounce occurs, we use the parameterized neutrino transport scheme (Liebendoerfer 2005). This scheme treats the electron capture as the only neutrino source and simplifies the neutrino transport by only including an instantaneous absorption/emission. The neutrino also affects the hydrodynamics through its pressure in the neutrino-opaque region as an ideal degenerate Fermi gas. To estimate the expected electron capture at high density, we use the fitting table in Abdikamalov et al. (2010), which contains the Y_e as a function of density. The electron fraction of the matter is instantaneously converted to the value given by the table, where the net change of electron capture is treated as neutrino source. After bounce, we switch to the Advanced Leakage Scheme (Perego et al. 2016). This scheme can be regarded as the extension of the leakage scheme (Rosswog & Liebendoerfer 2003), but is a simplified scheme of the Isotropic Diffusion Source Approximation (IDSA; Liebendoerfer et al. 2009). This is because this scheme treats the neutrino number fraction and mean energy as independent variables, as in IDSA. But in evolving to the new state, in the neutrino sector, it always assumes the new state inclines toward to the diffusion limit in the optically thin zones or the trapped limit in the optically thick zones. This guarantees that the scheme can approach asymptotically to a solution for an arbitrary timestep. This can bypass the difficulty of finding a new state in the original version of IDSA where occasionally no solution is found in zones where rigorous motion or discontinuities exist. In our simulations, we use 10 energy bands of neutrinos from 3 to 300 MeV in a logarithmic increasing band size. Since we want to understand the general properties of how the collapse takes place, we include only ν_e and $\nu_{\bar{e}}$ in our calculation with only two absorption/emission channels and four scattering channels, namely:

$$n + \nu_e \leftrightarrow p + e^-, \tag{8}$$

$$p - + \nu_{\bar{e}} \leftrightarrow n + e^+, \tag{9}$$

for the absorption/emission, and

$$n + \nu_i \leftrightarrow n + \nu_i, \tag{10}$$

$$p + \nu_i \leftrightarrow p + \nu_i, \tag{11}$$

$$\alpha + \nu_i \leftrightarrow \alpha + \nu_i, \tag{12}$$

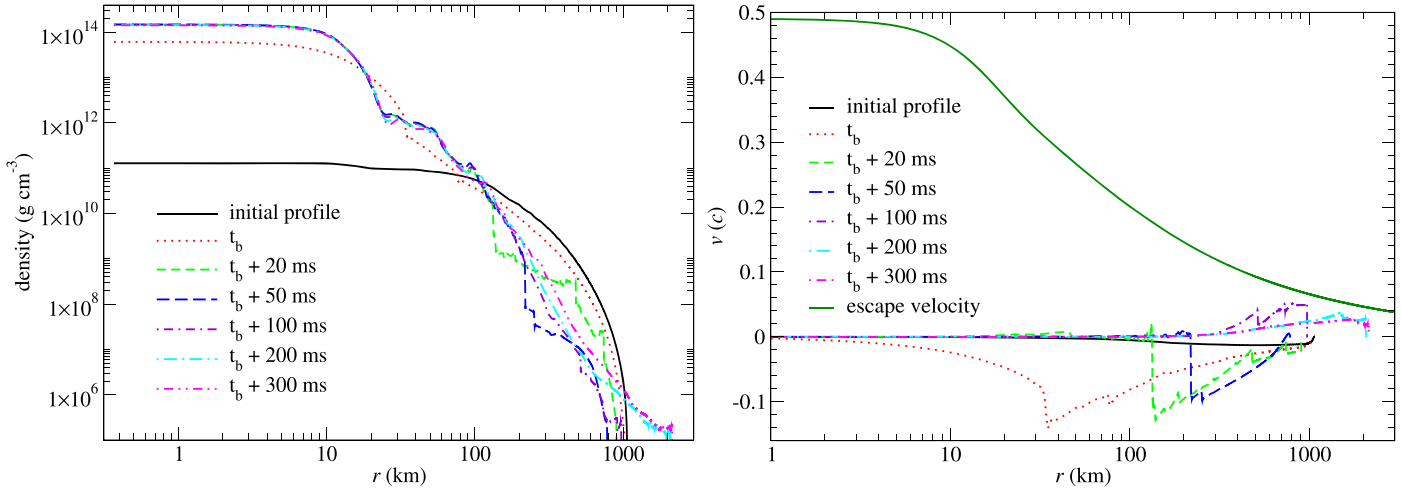

Figure 25. (Left panel) The density profiles of model c3-10000-N at the start of simulation (the same profile as it ends in the two-dimensional simulation), at the bounce, 20, 50, 100, 200, and 300 ms after bounce. (Right panel) Similar to left panel but for the velocity profiles.

Table 4
The Input Physics and the Choices of Physics Models in Simulations

Input Physics	Physics Model
Spatial discretization	Fifth-order Weighted Essentially Non-Oscillatory Scheme (Barth & Deconinck 1999)
Time discretization	Five-step Third-order Non-Strong Stability Preserved Runge–Kutta Scheme (Wang & Spiteri 2007)
Baryonic matter EOS	HShen EOS (Shen et al. 1998)
Pre-bounce electron capture	Fitting table from direct Boltzmann transport (Dessart et al. 2006; Abdikamalov et al. 2010)
Pre-bounce neutrino transport	Parameterized neutrino transport (Liebendoerfer 2005)
Post-bounce neutrino transport	Advanced leakage scheme (ALS) (Perego et al. 2016)

$$\text{ion} + \nu_i \leftrightarrow \text{ion} + \nu_i, \tag{13}$$

respectively. We use the rate formulae given in Bruenn (1985). Pair neutrino and neutrino bremmstrahlung are not included in this calculation. But these processes are less important compare to the channels included; although, we note that for a long-term simulation such as neutron-star cooling, these two channels gradually dominate over the first two absorption-emission channels.

Since the advanced leakage scheme does not include neutrino cooling, which is an important channel for the proto-neutron star to lose energy effectively after the neutrinosphere has been settled, we only run the simulations until ∼200 ms after bounce, to extract the neutrino signals.

In the left panel of Figure 25, we plot the density profiles of one of the collapse models c3-10000-N at the beginning of the one-dimensional simulation, at bounce, and 25 and 50 ms after bounce. At the beginning (the end of the two-dimensional simulations in the deflagration phase), the core starts with a flat density profile. But the inner core first contracts to reach nuclear density due to the loss of pressure by electron capture. At bounce, a stiff core made of nuclear matter at density around 3×10^{14} g cm^{-3} is formed. The inner envelope shows a steep density gradient showing that it is still falling onto the neutron star. The outer envelope does not change much. At 20 ms after bounce, the neutron star core reaches an equilibrium state in density, while the accretion of matter of the inner envelope creates a layer outside the neutron star. At around 10^{12} g cm^{-3}, strong fluctuations of density appear due to the tension between the infalling matter from the outer envelope and the stabilized inner envelope. At 50 ms after bounce, the neutron star has a static state envelope about 200 km. The remaining envelope has also contracted significantly to about 500 km, about half of its initial radius ≈1200 km. At 100 ms after bounce onward, no significant change in the density profile of the neutron star is observed up to 200 km. But there is still observable motion of the surface showing expansion. The cusps in the profiles also disappear.

In the right panel of Figure 25, we plot the velocity profiles for the same model, similar to the left panel. At the beginning, the star is having a homologous contraction with a maximum velocity about $1.3 \times 10^{-2}c$ at about 500 km. At bounce, we can see that a neutron star core close to static is formed with a size of about 15 km. Outside of the neutron star, there is an infalling envelope with a maximum velocity about $0.2c$. The infalling envelope also preserves the homologous velocity profile. Through shock heating, the material that has fallen on the neutron star quickly finds a hydrostatic equilibrium state. By examining the velocity profile at 20 ms after bounce, the bounce shock reaches about 100 km from the core, with a slightly lower infalling velocity about $0.16c$. There is outgoing matter in the profile at 50 ms after bounce. This shows that the shock has reached the region where density is low enough for the density gradient becomes large enough, so that the shock strength increases again when it propagates. The infalling velocity has decreased to $\approx 0.12c$. Once the accretion shock reaches the surface, since there is no further matter to suppress the expansion of matter, it creates a high-velocity flow near the surface. Some ejecta has a velocity exceeding the escape velocity. Such ejecta is likely to make the event dim and

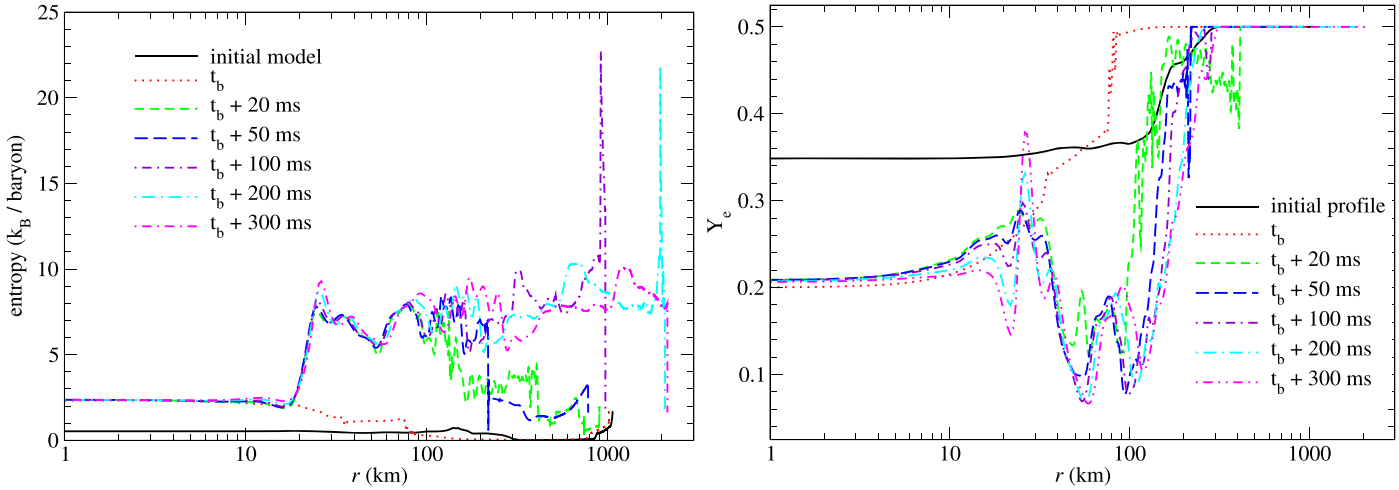

Figure 26. (Left panel) The entropy profiles of the benchmark ECSN model at the beginning, at bounce, and at 20, 50, 100, 200, and 300 ms after bounce. (Right panel) The Y_e profiles of the benchmark ECSN model at the beginning, at bounce, and at 20, 50, 100, 200, and 300 ms after bounce.

rapidly transient due to its high velocity and low ejecta mass. After the high-velocity matter is ejected, the material becomes bounded.

In Figure 26, we plot the entropy profiles similar to Figure 25. At the beginning, the whole star has almost a constant entropy $\approx$0.5 k_B per baryon, except near the surface. This is related to the initial flame put in by hand. The initial flame perturbs the initial hydrostatic equilibrium of the star. At bounce, the whole star reaches a constant entropy about 3 k_B per baryon. There is a cusp near the neutron star by the shock interaction. Similar to the velocity profiles, the quasi-static neutron star core has a constant entropy. At 20 ms, there is a significant rise of entropy to about 10 k_B per baryon in the newly accreted layer from 10 to 80 km. The high-entropy region can be compared with the velocity profile, which is the region that comes to a rest after it is deposited on the neutron star surface. At 50 ms, the shock has reached 200 km, and a high-entropy domain forms up to about 110 km. This is consistent with the literature that the neutrino heating is essential in producing high-entropy matter, which is supposed to be found in the ejecta. At 100 ms onwards, there is no significant change to the entropy profiles where a flat constant entropy zone is created in the envelope. At 100 ms after bounce, the ejecta has an entropy peak as high as $\sim$20 k_B per baryon.

In the right panel of Figure 26, we plot the Y_e profiles of the ECSN model similar to previous plots at the same time slice. The beginning Y_e profile is directly imported from the collapsing model in the main text. So, the core has reached a minimum of $\sim$0.35 and gradually increases at 100 km up to 0.45. No electron capture takes place beyond 200 km, where the deflagration has not yet reached the matter. At bounce, the core Y_e reaches 0.2 and gradually increases to 0.35 at $\sim$60 km, and up to 0.5 at 80 km. The locally higher Y_e from 80 to 200 km is because of the advection of matter. The high-Y_e matter falls inwards, but it has not reached the density for electron capture, so locally it looks like the Y_e increases by itself. After bounce, the shock and the consequent neutrino interactions influence the Y_e distribution. The high temperature allows rapid neutrino emission, which creates a trough of Y_e from 30 to 100 km. Ripples of Y_e appear due to the finite partitioning of neutrino energy band. As the shock propagates outwards, at 100, 200 and then 300 ms, we can see that the trough widens. Furthermore, the neutrinos, which diffuse outwards outside the neutrinosphere, smooth out the Y_e fluctuations created by the acoustic waves right after bounce.

In the left panel of Figure 27, we plot the neutrino energy spectra of the same model, similar to Figure 25. The number flux is taken at 300 km from the neutron star core. The number reaching the Earth can be scaled accordingly. There is no data for the initial model because no matter has reached nuclear density. At bounce, one can see the ν_e already has a spectrum comparable with the thermal spectrum. But the $\nu_{\bar{e}}$ spectrum is still extremely low. At 25 ms after bounce, ν_e has relaxed with a lower high-energy ν_e since the neutrinosphere is, in general, farther from center, which has a lower temperature. The $\nu_{\bar{e}}$ has also settled down to a thermal distribution. At 50 ms, both types of neutrinos have reached an equilibrium distribution. There are more low-energy ν_e but more high energy $\nu_{\bar{e}}$.

In the right panel of Figure 27, we plot the ν_e and $\nu_{\bar{e}}$ luminosity against time for the same model. The neutrino signal from an accretion-induced collapse of a WD into a neutron star is also plotted for comparison. The accretion induce collapse assumes a simple collapse of a Chandrasekhar mass isothermal WD due to an initial reduction of Y_e. It can be seen that, qualitatively, the two models are similar. At the beginning, a strong pulse of ν_e is emitted. But as the neutrinosphere of different energy bands starts to form, the neutrino emission drops. After a few expansions of the envelope, it reaches an equilibrium value of about 2×10^{52} erg s^{-1}. One minor difference is that the ONeMg case shows more oscillations than the cold AIC case. The $\nu_{\bar{e}}$ shows a similar behavior. It has a much lower luminosity. Consistent with the literature, the first peak appears later than the ν_e peak, about 20 ms after. The ONeMg model has about 50% higher $\nu_{\bar{e}}$ flux than the cold AIC model.

At last, we plot in Figure 28 the neutrino number flux profile at 100, 200, and 300 ms after bounce for both ν_e (solid line) and $\nu_{\bar{e}}$ (dashed line). For low-energy bands (3–8 MeV), ν_e is the dominant species. They are mostly created just outside the NS surface. No neutrino absorption can be seen, and most neutrinos are produced within the innermost 100 km. On the contrary, $\nu_{\bar{e}}$ is completely not produced in the NS and is gradually produced in the shock-heated matter outside the NS. Its number emission is at least one order of magnitude lower. However, as neutrino energy increases, the drop of ν_e number

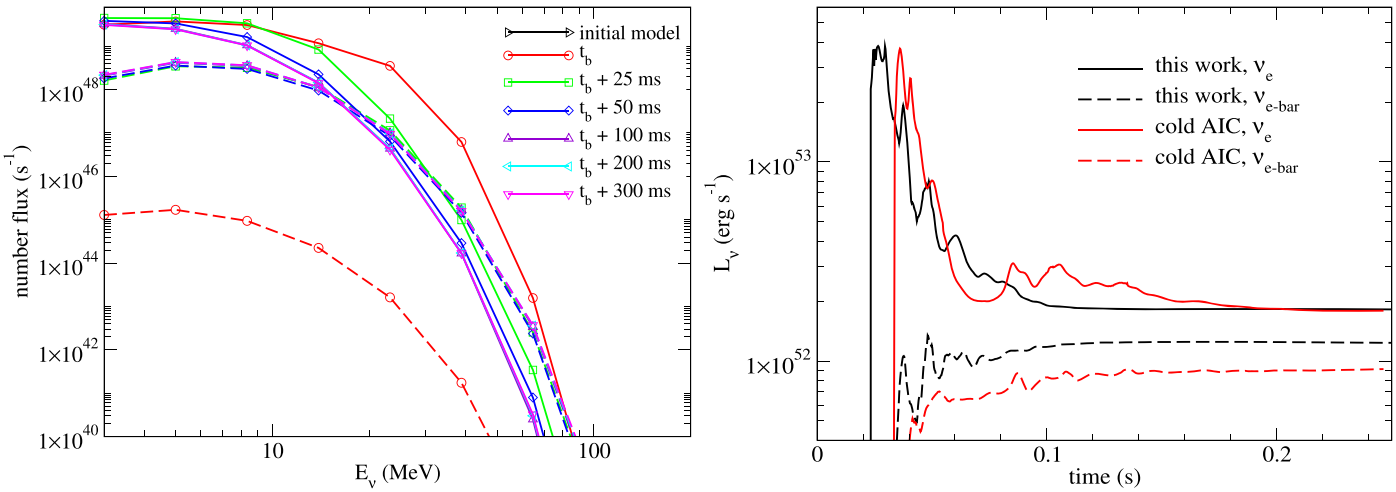

Figure 27. (Left panel) Similar to the left panel but for the free streaming neutrino flux. The solid (dashed) line stands for the ν_e ($\nu_{\bar{e}}$) flux at 300 km from the NS core. (Right panel) The ν_e and $\nu_{\bar{e}}$ luminosity for the Model c3-10000-N. The sample neutrino luminosity from the collapse of an AIC is included for comparison.

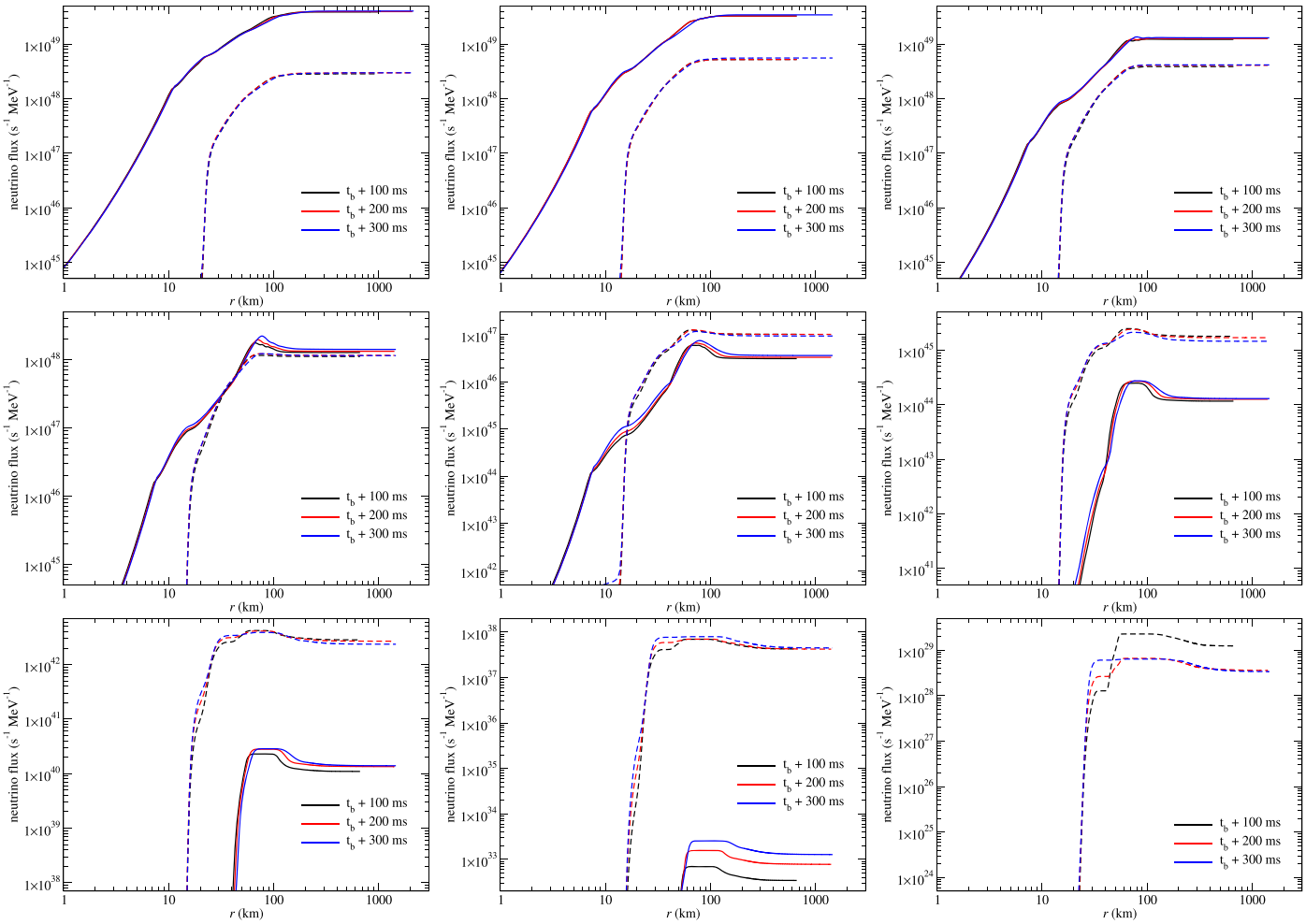

Figure 28. The ν_e (solid line) and $\nu_{\bar{e}}$ (dashed line) number flux profile at 100 (black), 200 (red), and 300 (blue) ms after bounce. The neutrino energy bands include 3, 5, 8, 14, 23, 39, 65, 108, and 180 MeV.

flux is faster than the drop of $\nu_{\bar{e}}$. This is because the creation of $\nu_{\bar{e}}$ is limited to places where positrons can be freely formed. Notice that to create ν_e, the electron should have a chemical potential not only for the creation of itself, but also for the mass difference between n and p ($\sim$1.2 MeV). At 20–100 km, the density has already dropped below 10^{12} g cm^{-3}. This means the nucleons are no longer degenerate, and thus, they have a much lower chemical potential than those in the core. So, this leaves a strong cutoff in the high-energy ν_e. On the other hand, the production of $\nu_{\bar{e}}$ is aided by the energy difference for the same origin. So, its drop in number flux is less steep than ν_e.

For a higher neutrino energy, more features can be observed. At 14, 23, and 39 MeV, both ν_e and $\nu_{\bar{e}}$ show a first increasing function up to 80 km and then slightly drop until 100 km. The change of ν_e is larger than that of $\nu_{\bar{e}}$, showing that more ν_e is absorbed. As a result, this explains the local bump of Y_e in the right panel of Figure 26.

For even higher neutrino energy (65, 108, and 180 MeV), the drops of ν_e become so rapid that it becomes irrelevant to the neutrino transport and the global neutrino flux. $\nu_{\bar{e}}$ also shows a similar feature but with lower strength. However, they are also unimportant to the global neutrino population.

ORCID iDs

Shing-Chi Leung https://orcid.org/0000-0002-4972-3803
Ken'ichi Nomoto https://orcid.org/0000-0001-9553-0685

References

Abdikamalov, E. B., Ott, C. D., Rezzolla, L., et al. 2010, PhRvD, 81, 044012
Arnett, D. 1996, Supernovae and Nucleosynthesis: An Investigation of the History of Matter from the Big Bang to the Present (Princeton: Princeton University Press)
Barth, T. J., & Deconinck, H. 1999, Lecture Notes in Computational Science and Engineering 9: High-Order Methods for Computational Physics (Berlin: Springer)
Bell, J. B., Day, M. S., Rendleman, C. A., Woosley, S. E., & Zingale, M. 2004a, ApJ, 606, 1029
Bell, J. B., Day, M. S., Rendleman, C. A., Woosley, S. E., & Zingale, M. 2004b, ApJ, 608, 883
Bruenn, S. W. 1985, ApJS, 58, 771
Canal, R., & Schatzman, E. 1976, A&A, 46, 229
Chechetkin, V. M., Gershtein, S. S., Imshennik, V. S., Ivanova, L. N., & Khlopov, M. I. 1980, Ap&SS, 67, 61
Dessart, L., Burrows, A., Ott, C., et al. 2006, ApJ, 644, 1063
Doherty, C. L., Gil-Pons, P., Siess, L., Lattanzio, J. C., & Lau, H. H. B. 2015, MNRAS, 446, 2599
Fink, M., Kromer, M., Seitenzahl, I. R., et al. 2014, MNRAS, 438, 1762
Gershteĭn, S. S., Ivanova, L. N., Imshennik, V. S., Khlopov, M. Y., & Chechetkin, V. M. 1977, JETPL, 26, 178
Hashimoto, M., Iwamoto, K., & Nomoto, K. 1993, ApJL, 414, L105
Hicks, E. P. 2015, ApJL, 414, L105
Jones, S., Hirschi, R., Nomoto, K., et al. 2013, ApJ, 772, 150
Jones, S., Hirschi, R., & Nomoto, K. 2014, ApJ, 797, 83
Jones, S., Röpke, F. K., Fryer, C., et al. 2019, A&A, 622, A74
Jones, S., Röpke, F. K., Pakmor, R., et al. 2016, A&A, 593, A72
Karakas, A. I. 2017, in Handbook of Supernovae, ed. A. W. Alsabti & P. Murdin (Cham: Springer), 461
Khokhlov, A. M., Oran, E. S., & Wheeler, J. C. 1997, ApJ, 478, 678
Kim, J., Kim, H. I., Choptuik, M. W., & Lee, H. M. 2012, MNRAS, 424, 830
Kitamura, H. 2000, ApJ, 539, 888
Langanke, K., & Martinez-Pinedo, G. 2001, ADNDT, 79, 1
Langer, N. 2012, ARA&A, 50, 107
Leung, S.-C., Chu, M.-C., & Lin, L.-M. 2015a, MNRAS, 454, 1238
Leung, S.-C., Chu, M.-C., & Lin, L.-M. 2015b, ApJ, 812, 110
Leung, S.-C., & Nomoto, K. 2017, in JPS Conf. Proc., 14th Int. Symp. Nuclei in the Cosmos (NIC2016) JPS Conference Proceedings, ed. S. Kubono et al. (Tokyo: The Physical Society of Japan), 020506
Leung, S.-C., & Nomoto, K. 2018, ApJ, 861, 143
Liebendoerfer, M. 2005, ApJ, 633, 1042
Liebendoerfer, M., Whitehouse, S. C., & Fischer, T. 2009, ApJ, 698, 1174
Livne, E., & Arnett, D. 1993, ApJL, 415, L107
Long, M., Jordan, G. C. I., van Rossum, D. R., et al. 2014, ApJ, 789, 103
Ma, H., Woosley, S. E., Malone, C. M., Almgren, A., & Bell, J. 2013, ApJ, 771, 58
Miyaji, S., & Nomoto, K. 1987, ApJ, 318, 307
Miyaji, S., Nomoto, K., Yokoi, K., & Sugimoto, D. 1980, PASJ, 32, 303
Mochkovitch, R., & Livio, M. 1989, A&A, 209, 111
Nabi, J.-U., & Klapdor-Kleingrothaus, H. V. 1999, ADNDT, 71, 149
Niemeyer, J. C., Hillebrandt, W., & Woosley, S. E. 1995, ApJ, 452, 979
Nomoto, K. 1982, ApJ, 253, 798
Nomoto, K. 1984, ApJ, 277, 791
Nomoto, K. 1987, ApJ, 322, 206
Nomoto, K., & Hashimoto, M. 1988, PhR, 163, 13
Nomoto, K., Kobayashi, C., & Tominaga, N. 2013, ARA&A, 51, 457
Nomoto, K., & Kondo, Y. 1991, ApJL, 367, L19
Nomoto, K., & Leung, S.-C. 2017a, in Handbook of Supernovae, ed. A. W. Alsabti & P. Murdin (Cham: Springer), 483
Nomoto, K., & Leung, S.-C. 2017b, in Handbook of Supernovae, ed. A. W. Alsabti & P. Murdin (Cham: Springer), 1275
Nomoto, K., Sparks, W. M., Fesen, R. A., et al. 1982, Natur, 299, 803
Nomoto, K., Sugimoto, D., & Neo, S. 1976, Ap&SS, 39, L37
Osher, S., & Sethian, J. A. 1988, JCoPh, 79, 12
Perego, A., Cabezon, R. M., & Käppeli, R. 2016, ApJS, 223, 22
Peter, N. 1999, JPM, 384, 107
Plewa, T. 2007, ApJ, 657, 942
Pocheau, A. 1994, PhRvE, 49, 1109
Pumo, M. L., Turatto, M., Botticella, M. T., et al. 2009, ApJL, 705, L138
Raddi, R., Hollands, M. A., Koester, D., et al. 2018, ApJ, 858, 3
Reinecke, M., Hillebrandt, W., & Niemeyer, J. C. 1999, A&A, 347, 739
Reinecke, M., Hillebrandt, W., & Niemeyer, J. C. 2002a, A&A, 386, 936
Reinecke, M., Hillebrandt, W., & Niemeyer, J. C. 2002b, A&A, 391, 1167
Röpke, F. K. 2005, A&A, 432, 969
Röpke, F. K., & Hillebrandt, W. 2005, A&A, 431, 635
Röpke, F. K., Hillebrandt, W., & Niemeyer, J. C. 2004a, A&A, 420, 411
Röpke, F. K., Hillebrandt, W., & Niemeyer, J. C. 2004b, A&A, 421, 783
Röpke, F. K., Hillebrandt, W., Schmidt, W., et al. 2007, ApJ, 668, 1132
Rosswog, S., & Liebendoerfer, M. 2003, MNRAS, 342, 673
Schmidt, W., Niemeyer, J. C., Hillebrndt, W., & Roepke, F. K. 2006, A&A, 450, 283
Schwab, J., Martinez-Rodriguez, H., Piro, A. L., & Badenes, C. 2017, ApJ, 851, 105
Schwab, J., Quataert, E., & Bildsten, L. 2015, MNRAS, 453, 1910
Seitenzahl, I. R., Ropeke, F. K., Fink, M., & Pakmor, R. 2010, MNRAS, 407, 2297
Shen, H., Toki, H., Oyamatsu, K., & Sumiyoshi, K. 1998, NuPhA, 637, 435
Siess, L. 2007, A&A, 476, 893
Sugimoto, K., & Nomoto, K. 1980, SSRv, 25, 155
Suzuki, T., Toko, H., & Nomoto, K. 2016, ApJ, 817, 163
Takahashi, K., Yoshida, T., & Umeda, H. 2013, ApJ, 771, 28
Timmes, F. X. 1999, ApJ, 124, 241
Timmes, F. X., & Arnett, D. 1999, ApJ, 125, 277
Timmes, F. X., & Woosley, S. E. 1992, ApJ, 396, 649
Toki, H., Suzuji, T., Nomoto, K., et al. 2013, PhRvC, 88, 015806
Townsley, D. M., Calder, A. M., Asida, S. M., et al. 2007, ApJ, 668, 1118
Umeda, H., Nomoto, K., Yamaoka, H., & Wanajo, S. 1999, ApJ, 513, 861
Wanajo, S., Müller, B., Janka, H.-T., & Heger, A. 2018, ApJ, 852, 40
Wang, R., & Spiteri, R. J. 2007, SJNA, 45, 1871
Woosley, S. E. 1997, ApJ, 476, 801
Woosley, S. E., & Heger, A. 2015, ApJ, 810, 34
Yoon, S.-C., Podsiadlowski, Ph., & Rosswog, S. 2007, MNRAS, 380, 993